

Exploring the Potential of Long Short-Term Memory Networks for Improving Understanding of Continental- and Regional-Scale Snowpack Dynamics

Yuan-Heng Wang¹, Hoshin V Gupta¹, Xubin Zeng¹ and Guo-Yue Niu¹

¹Department of Hydrology and Atmospheric Sciences, The University of Arizona, Tucson, AZ 85721, USA

Corresponding author: Yuan-Heng Wang (yhwang0730@email.arizona.edu)

Key Points

- 1) A trained CONUS-wide LSTM is capable of providing almost as good performance as a regionally trained one
- 2) The CONUS-wide LSTM outperforms a regionally trained SNOW17, and a SNOW17 model calibrated locally to each pixel across the domain
- 3) The LSTM exhibits better spatial transferability than SNOW17, reinforcing the advantages of structure learning over parameter learning.

Keywords

Deep Learning; LSTMs; Snow accumulation and melt; SNOW17

Abstract

Accurate estimation of the spatio-temporal distribution of snow water equivalent is essential given its global importance for understanding climate dynamics and climate change, and as a source of fresh water. Here, we explore the potential of using the Long Short-Term Memory (LSTM) network for continental and regional scale modeling of daily snow accumulation and melt dynamics at 4-km pixel resolution across the conterminous US (CONUS). To reduce training costs (data are available for ~0.31 million snowy pixels), we combine spatial sampling with stagewise model development, whereby the network is first pretrained across the entire CONUS and then subjected to regional fine-tuning. Accordingly, model evaluation is focused on out-of-sample predictive performance across space (analogous to the prediction in ungauged basins problem). We find that, given identical inputs (precipitation, temperature and elevation), a single CONUS-wide LSTM provides significantly better spatio-temporal generalization than a regionally calibrated version of the physical-conceptual temperature-index-based SNOW17 model. Adding more meteorological information (dew point temperature, vapor pressure deficit, longwave radiation and shortwave radiation) further improves model performance, while rendering redundant the local information provided by elevation. Overall, the LSTM exhibits better transferability than SNOW17 to locations that were *not* included in the training data set, reinforcing the advantages of structure learning over parameter learning. Our results suggest that an LSTM-based approach could be used to develop continental/global-scale systems for modeling snow dynamics.

Plain Language Summary

Understanding the spatio-temporal distribution of water in the snowpack (known as snow water equivalent) is very important for understanding climate dynamics and climate change, and for forecasting and management of global water supplies. In this study, we use Deep Learning (DL) to model snow accumulation and melt at 4-km pixel-scale resolution across the conterminous US (CONUS). Long Short-Term Memory (LSTM) networks are developed at both continental- and regional-scale, by combining spatial pixel sampling and stagewise network pre-training/fine-tuning. We benchmark out-of-sample predictive performance against the physical-conceptual temperature-index-based SNOW17 model, and find that LSTM networks significantly outperform calibrated versions of the SNOW17 model when given identical information. Further, when provided with additional meteorological information, performance of the LSTM is improved. The LSTM models also exhibits better transferability than the SNOW17, indicating the potential for future development of a DL-based system for modeling continental/global-scale snow dynamics.

1 **1. Introduction**

2 **1.1 The Problem of Continental-Scale Estimation of Snow Water Equivalent**

3 [1] Accurate monitoring of the large-scale dynamics of snowpack is essential for understanding
4 the details of climate dynamics and climate change (*Robinson et al., 1993*). Warming under a
5 changing climate is expected to cause snowpack to melt earlier in the year (*Zeng et al., 2018; Xiao,*
6 *2021*) and to reduce the amount of water stored as snow (*Nijssen et al., 2001; Musselman et al.,*
7 *2021*). This is expected to have broad and potentially severe impacts to ecosystem productivity
8 (*Boisvenue and Running 2006*), winter flood risk (*Musselman et al., 2018*), groundwater recharge
9 (*Ford et al., 2020*), agriculture and food security (*Shindell et al., 2012; Qin et al., 2020*), wildfire
10 hazard (*Westerling et al., 2016*), and frequency and severity of drought (*Arevalo et al., 2021*). In
11 western North America, snow is the primary source of water and streamflow (*Li et al., 2017*),
12 while globally it supports the water supply needs for more than one billion people (*Barnett et al.,*
13 *2005*). Therefore, having accurate estimates of the quantity of water stored in snowpack, called
14 snow water equivalent (SWE), is critical for the forecasting and management of water supply and
15 hydropower (*Mankin et al., 2015; Bales et al., 2016*).

16 [2] Several different physically-based snow models have been developed to simulate the co-
17 evolution of mass and energy within the snowpack system, and to thereby provide estimates of
18 SWE. Examples include the temperature-index based SNOW-17 model (*Anderson 1973*), UEB
19 (*Tarboton and Luce 1996*), SAST (*Jin et al. 1999*), ESCIMO (*Strasser et al. 2002*), and
20 SNOWCAN (*Tribbeck et al. 2004*). More sophisticated snow models that focus on advanced
21 representations of stratigraphy or internal dynamics (i.e., grain structure etc.) of the snowpack
22 include Crocus (*Brun et al., 1992*), and the physics-based SNOWPACK model (*Bartelt and*
23 *Lehning, 2002*). In practice, modelers typically use simpler physical-conceptual land-surface
24 representations such as VIC (*Liang et al., 1994*) to estimate the broad changes in snowpack that
25 might be expected under climate change. Meanwhile, the iSNOBAL model has been the modeling
26 engine for spatially distributed SWE estimation within the Airborne Snow Observatory (ASO)
27 product (*Marks et al., 1999*).

28 [3] Nonetheless, the predictive performance of all such models depends on whether or not their
29 representations of the underlying data-generating processes are adequate. To address poor
30 predictive performance stemming from inadequate physical representations, modelers have
31 explored a full spectrum of explicit process hypotheses (Noah-MP; *Niu et al., 2011*), synthesized
32 multiple working hypotheses into a unifying modeling framework (SUMMA; *Clark et al., 2010;*
33 *Clark et al., 2016*), linked the parameter values to local basin attributes by imposing spatial
34 regularization constraints (*Pokhrel et al., 2008*) via parameter transfer functions (mHM;
35 *Samaniego et al., 2010*), and explored implementations at finer spatial resolutions (HydroBlocks;
36 *Chaney et al., 2016*). However, a potential downside of such methods is the large computational
37 demands imposed when conducting simulations at practically useful resolutions over large spatial
38 extents.

39 [4] Following a complementary approach, statistical data-driven approaches (such as multiple
40 linear regression and binary regression trees) have also been widely used to generate estimates of
41 targeted snow variables at continental- and watershed-scales by exploiting the information
42 provided by field measurements in conjunction with observed physiographic and meteorological
43 covariates (see the review in *Broxton et al., 2019*). Many studies have explored ML approaches

44 to the estimation of snow variables (e.g., snow depth, snowfall, SWE and the fractional snow cover)
45 include the application of Random Forest and Support Vector Machine methods, using a variety
46 of input data such as satellite sensors (*Kuter et al. 2018; Kuter, 2020; Ehsani et al., 2021*),
47 terrestrial laser scanners (*Revuelto et al., 2020*), land models (*Snauffer et al., 2018*), and ground
48 observations (*Tabari et al., 2010; Buckingham et al., 2015; Gharaei-Manesh et al., 2016*). The
49 results of these efforts, which draw upon recent advances in machine learning (ML), and
50 particularly deep learning, suggest that ML-based methods have the potential to outperform state-
51 of-the-art techniques for many sophisticated domain problems (*Krazert et al., 2019a*).

52 [5] In the context of snow hydrology, the artificial neural network (ANN; sometimes called the
53 feedforward multilayer perceptron) has been used to improve the estimation of SWE in different
54 ways, such as the Snow Water Artificial Neural Network Modelling (SWANN) system (*Broxton
55 et al., 2017*). *Snauffer et al. (2018)* used ANNs for multi-source data fusion, using SWE data from
56 reanalysis products and manual snow surveys as network inputs, and reported improvements in
57 the quality of gridded SWE products. *Broxton et al. (2019)* combined aerial remotely-sensed maps
58 of snow depth with snow density maps generated via artificial neural network (ANN) processing
59 of field measurements to improve the estimation of SWE. These successes can be attributed to the
60 ability of ANNs to learn the nonlinear nature of the relationships between the relevant variables,
61 resulting in improved performance over traditional statistical methods (*Czyzowska-Wisniewski et
62 al., 2015*). Recently, the studies of how to improve SWE estimates has explored the use of multiple
63 data types and a variety of features derived from meteorological quantities as inputs to the training
64 of ensemble MLP models (*Odry et al., 2020; Ntokas et al., 2021*). In general, it seems reasonable
65 that ML-based methods should be able to provide relevant and useful information over large spatial
66 domains; see for example the pixel scale return-level design maps of SWE developed for modeling
67 for snowmelt-driven floods over the entire CONUS (*Cho and Jacobs, 2020; Wetly and Zeng, 2021*).

68 **1.2 The Potential offered by Deep Learning**

69 [6] Deep learning (DL) has recently been proposed as a powerful strategy for hydrological
70 modeling and time-series prediction (*Shen, 2018; Shen et al., 2018*). In particular, the long short-
71 term memory network (LSTM; *Hochreiter and Schmidhuber 1997*) has been reported to
72 outperform the traditional ANN approach, provided that sufficient data is available for model
73 development (*Wunsch et al., 2021*). In particular, *Kratzert et al. (2018)* showed that the knowledge
74 encapsulated by the generic pre-trained LSTM network can be transferred to different locations in
75 the context of rainfall-runoff modeling. By initializing the LSTM network parameters to those of
76 the pre-trained model, and by conducting subsequent local fine-tuning (*Yosinski et al., 2014;
77 Kratzert et al. (2018)*), it should be possible to reduce local data requirements, thereby facilitating a
78 variety of hydrological applications such as regionalization and prediction in ungauged basins
79 (PUB; *Hrachowitz et al., 2013; Sivapalan et al., 2003*).

80 [7] For rainfall-runoff modeling, *Kratzert et al. (2019b)* showed that a single regionally-trained
81 LSTM network can provide better basin-specific predictions than traditional hydrological models
82 locally calibrated basin-by-basin. Further, when the regionally-trained LSTM was applied to
83 basins whose data was not used for model development (i.e., effectively treating them as
84 “*ungauged*” basins) it performed, on average, better than instances of the Sacramento Soil
85 Moisture Accounting Model (SAC-SMA) or the NOAA National Water Model that were directly
86 calibrated to those same basins (*Kratzert et al., 2019a*). These asymmetrical comparisons illustrate
87 the ability of a standard LSTM architecture to learn a model structure that performs better than a

88 “*physics-based*” model, by effectively exploiting the relevant information available in the input-
89 output data.

90 **1.3 Problem Definition, Objectives, and Scope of this Work**

91 [8] This study explores the capability of LSTMs for modeling the dynamics of snow
92 accumulation and melt. The main goal is to achieve accurate estimates of SWE over a large spatial
93 domain by exploiting available pixel-scale datasets while maintaining a reasonable level of
94 computational cost. Our approach involves step-wise training (*Kratzert et al., 2018*) of an LSTM
95 network using a subset of pixel-scale data sampled across the entire CONUS, where we first use
96 CONUS-wide network pre-training to initialize the network parameters, followed by regional fine-
97 tuning of the network. In particular, our modeling experiments were designed to examine the
98 spatial transferability of predictive performance, thereby facilitating the application of PUB in the
99 context of snow hydrology (*Kratzert et al., 2019a*).

100 [9] To explore the best achievable performance for SWE modeling, we train the LSTM networks
101 using different combinations of “available” input data and benchmark the network performance
102 against the temperature-index-based SNOW17 model (*Anderson, 2006*; hereafter SN17). Our main
103 interests are in (1) whether the LSTM can outperform the SN17 model used by the National
104 Weather Service River Forecast Center (NWS RFC) for operational hydrologic prediction, and (2)
105 to what extent the performance of the LSTM is affected by different system structure hypotheses,
106 implemented as continental, regional and local training (calibration) strategies.

107 [10] The scope of our research goes beyond simply pursuing accurate modeling of SWE dynamics,
108 by investigating the possibilities of using LSTM-based ML as an upper benchmark in the context
109 of hypothesis testing (*Gong et al., 2013; Nearing et al., 2020*), that can be used to facilitate and
110 guide improvements to *physically-based* modeling of SWE dynamics. In section 2, we introduce
111 the LSTM-based and SN17 strategies for modeling snow, and discuss the data used for this study.
112 Section 3 discusses the details of our experimental design. In section 4 we present and discuss the
113 results. In section 5, we summarize our findings and discuss the outlook for future work.

114 **2. Methods**

115 **2.1 Models**

116 **2.1.1 Long Short-Term Memory Network (LSTM)**

117 [11] An LSTM network is a type of recurrent neural network that includes memory cells that have
118 the ability to store information over long time periods (*Figure S1*). These cells are subjected to
119 three “*gating*” operations that effectively control the weight gradients and facilitate the learning of
120 long-term dependencies (*Hochreiter and Schmidhuber, 1997*). Further, each memory cell
121 functions in a manner analogous to a “*state vector*” in a traditional dynamical systems model,
122 which makes the LSTM architecture an ideal candidate for developing models of dynamical
123 systems (*Krazert et al., 2018*); for a comprehensive hydrological interpretation of the LSTM
124 architecture, please refer to *Kratzert et al. (2018)*. In this study, we adopt the LSTM network
125 architecture as used by *Krazert et al. (2019b)* where the network architecture equations are
126 summarized in supplementary materials.

127 **2.1.2 Snow Accumulation and Ablation Model (SNOW17)**

128 [12] The NWS is the US agency responsible for short-term and long-term streamflow predictions
129 across the nation. The NWS RFC primarily uses the SN17 model (*Anderson, 2006*) for generating
130 operational forecasts of snow accumulation and melt in snow-dominated areas. SN17 is a
131 spatially-lumped process-based model that simulates snow accumulation and ablation. It requires
132 three input data sets; air temperature and precipitation data are used as meteorological inputs, while
133 information regarding elevation is used to compute atmospheric pressure. The model outputs
134 include a rain-plus-snowmelt time series, as well as SWE (*Figure S2*). In this work, we apply the
135 parsimonious point-scale assumption of full snow cover at the pixel-scale. Therefore, it is
136 configured as a physical-oriented empirical temperature index model. We adopt the model
137 structure and associated feasible parameter ranges (*Table 1*) presented by *He et al. (2011a,b)*.

138 **2.2 Data**

139 **2.2.1 Meteorological Input Forcing**

140 [13] In this study, the LSTM and SN17 models were driven by meteorological forcing at the daily
141 time scale. As inputs, we used daily values of precipitation, mean temperature, dewpoint
142 temperature, and vapor pressure deficit from the Parameter-Elevation Regressions on Independent
143 Slopes Model data set (PRISM; *Daly et al. 1994*). While PRISM data are more uncertain over
144 complex terrain (*Henn et al. 2018*), it is arguably the best gridded climate dataset available at this
145 time, particularly for the western CONUS. We also used hourly, 0.125° near-surface downward
146 longwave and shortwave radiation data from the near-real-time North American Land Data
147 Assimilation Phase 2 data set (NLDAS-2; *Xia et al., 2012*). The hourly downward longwave and
148 shortwave radiation data were first averaged to daily timescale and then resampled to 4-km
149 resolution using nearest-neighbor interpolation onto the resulting grid coordinate with respect to
150 PRISM.

151 **2.2.2 Snow Water Equivalent (SWE) Target Variables**

152 [14] As the target variable for LSTM training and for SNOW-17 calibration, and to evaluate the
153 simulation results, we used the University of Arizona (UA) ground-based daily 4-km SWE data
154 product (*Broxton et al., 2016; Zeng et al., 2018*). This data set was developed by assimilating in
155 situ measurements of SWE and/or snow depth at thousands of sites (*Broxton et al., 2016; Dawson
156 et al., 2017*) using 4-km gridded PRISM precipitation and temperature data (*Daly et al., 1994*)
157 over the CONUS. Accuracy and robustness of the UA snow product, and its use as a reference
158 continental snowpack data set, have been assessed via four rigorous evaluation studies including
159 point-to-point interpolation (*Broxton et al., 2016*), pixel-to-pixel interpolation (*Broxton et al.,
160 2016*), and evaluation against independent snow cover extent data and airborne lidar measurements
161 (*Dawson et al., 2018*). The UA SWE data product was found to align closely with the CONUS 1-
162 km SWE product from the Snow Data Assimilation System (SNODAS; *Barrett, 2003*) and to show
163 much better agreement with gamma SWE than the Special Sensor Microwave Imager and Sounder
164 (SSMIS) SWE and GlobSnow-2 SWE grid products for various land cover types and snow classes
165 (*Cho et al., 2020*).

166 **2.2.3 Static Features**

167 [15] To obtain gridded spatial maps of static land-surface characteristics, we used the open-source
168 Geospatial Data Abstraction Library (GDAL)'s `gdal_translate` command-line tool to perform
169 spatial reprojection of the Shuttle Radar Topography Mission (SRTM; *Jarvis et al. 2008*) digital

170 elevation model elevation data to 4-km resolution; this is consistent with the PRISM latitude–
171 longitude grid using average upscaling interpolation.

172 [16] The “majority” operation was used to upscale the 1-km MODIS land cover climatology
173 dataset to the 4-km resolution grid (*Broxton et al., 2014*). We defined forested pixels to be those
174 that included Evergreen Needleleaf, Evergreen Broadleaf, Deciduous Broadleaf, Mixed Forests,
175 and Woody Savannas, whereas the remaining land cover types were classified as Non-Forested
176 pixels.

177 **3. Experimental Approach**

178 **3.1 Study Region**

179 [17] All the studies reported in this paper were conducted at 4-km pixel-scale over the CONUS,
180 using a coordinate system and spatial coverage that is consistent with the PRISM meteorological
181 forcing and UA SWE datasets. Roughly 0.31 million pixels were identified to be “snowy” from a
182 total of approximately 0.46 million total pixels associated with the UA snow product data set. This
183 categorization of snowy pixels was based on the snowpack climatology, where any pixel with
184 median annual snowy season length less than 30 days, or median annual daily maximum SWE less
185 than 10 mm, was classified as being “non-snowy”, as shown in *Figure 1* (*Zeng et al., 2018*).

186 [18] Next, we selected five regions (shown in *Figure 1*) to explore the potential for using the
187 LSTM architecture as a regional modeling tool, where the objective was to simulate snow
188 accumulation and melt behavior over a large number of different pixels at the daily timescale.
189 Three western CONUS regions – the Colorado River Basin (hereafter CRB), Sierra Nevada
190 (hereafter SN), and Cascades (hereafter CC) – were selected based on the important role that
191 snowpack plays in contributing to their freshwater resources. The high elevation snowpack of the
192 Rocky Mountains is known to contribute about 70% of the annual runoff of the Colorado River
193 Basin (*Christensen et al., 2004*), while the Colorado River provides fresh water to over 40 million
194 people in seven states and two countries (*Deems et al., 2013*). Also, in the SN and CC mountains
195 (*Simpkins, 2018*), approximately 75% of freshwater originates from snow. To further ensure that
196 the selected regions cover as wide a range of characteristics as possible in terms of geographic
197 location, climatic regimes and local physiographic properties, we selected two additional USGS
198 first level regions, namely Ohio (hereafter OH) and Missouri (hereafter MO), designated by a two-
199 digit Hydrologic Unit Code (HUC).

200 [19] The five selected regions cover a variety of topography and land cover regimes. The pixel
201 aspect was derived from SRTM digital elevation model (at its original resolution), and a consistent
202 result was obtained by binning into eight directions; the two dominant aspects were determined to
203 be north and south-facing slopes, together occupying around 30% of the total pixels over the five
204 regions. For MO, the dominant aspect was determined to be north, and for the rest of the regions
205 the dominant aspect was determined to be south. OH, MO and CC have mean elevations below
206 1,500 m (low elevation zone), while CRB and SN are between 1,500 m and 2,500 m with 18.2%
207 and 16.3% pixels respectively having mean elevations above 2,500 m (high elevation zone; *Mote,*
208 *2006*). The OH, MO and CRB have relatively less percentage of forest pixel (about 36.6%, 3.81%,
209 9.69 respectively) whereas the SN and CC are recognized as being forest-dominated, with more
210 than half of the pixels classified as forested (about 52% and 83%). These factors are known to
211 exert strong controls on the energy balance during snowmelt (*Garvelmann et al., 2015*), and can
212 be highly variable in space and time (*Pohl et al., 2006*).

213 3.2 Experimental Design

214 [20] Data from the time period 1st October 1981 through 30th September 2000 were used for all
215 model development runs – i.e., SN17 calibration and LSTM training. For both the steps of
216 calibration/training and testing of the models, we used data from the same time period, but from
217 different spatially located pixels. In other words, our testing procedure evaluates the ability of each
218 model to extrapolate in space, which is analogous to the problem of prediction in ungauged basins
219 (*Hrachowitz et al., 2013; Sivapalan et al., 2003*). Note that it is computationally challenging (or
220 nearly impossible) to train either model (SN17 or LSTM) using data from the entire set of ~0.31
221 million snowy pixels; nor does it seem necessary. Instead, we use a process of sampling to select
222 different, but representative, subsets of pixels to be used for training and for testing, as described
223 in the following sections. As a precedent for this, *Huo et al (2019)* have shown (in the context of
224 sensitivity analysis) that the performance of a computationally intensive spatially distributed
225 model can be reliably assessed by using only a sample of ~5% of the total number of pixels
226 available over the CONUS.

227 [21] The study reported here was conducted in several stages. In the first experiment (Section
228 3.2.1), we trained both model architectures (LSTM and SN17) to represent snowmelt dynamics at
229 15,000 pixels selected randomly across the CONUS. This preliminary experiment had two
230 purposes: 1) To determine whether the LSTM architecture is able to learn a better mapping
231 relationship from inputs to outputs than the SN17 model, and 2) To examine whether the LSTM
232 network architecture is able to exploit the information provided by other meteorological variables
233 than those used by SN17, to achieve better model performance.

234 [22] Then, in the second experiment (Section 3.2.2), we evaluated both model architectures on a
235 different set of 15,000 pixels (none of which were used in the first experiment) but selected in such
236 a manner so as to provide equal representation to each of the five study regions mentioned above
237 –Ohio, Missouri, Colorado, Sierra Nevada and the Cascades. The goals of this experiment were:
238 1) To assess whether the model performance obtained in the first experiment remains consistent
239 when applied to another independent dataset, and 2) To examine the possibility of regional
240 differences in performance.

241 [23] In the third experiment (Section 3.2.3), we examined the transferability of LSTM-based
242 models across regions. The goal is to investigate the extent to which different spatial regions share
243 a common model structural representation.

244 3.2.1 Experiment 1: CONUS-wide modeling of snow accumulation and melt

245 [24] The purpose of the first experiment was to investigate the potential of using the LSTM
246 machine-learning architecture as an alternative to the SN17 model structure for pixel-based
247 CONUS-wide modeling of snow accumulation and melt. To this end, one single LSTM network
248 was trained using input-output data from the entire country. Since training the network using data
249 from more than 0.31 million pixels would be computationally prohibitive, we randomly selected
250 15,000 pixels from “snowy” areas across the CONUS (Figure 3). The goal was to obtain a
251 representative subset of ~5% of the total number of possible snowy pixels. Then, to train the LSTM
252 network, we constructed 15 bootstrap sample sets, each consisting of 1000 different pixels
253 randomly selected from the total set of 15,000 snowy pixels. We collectively refer to these 15
254 bootstrapped sets as *Pixel Set A*.

255 [25] The LSTM network was trained for a total of 15 epochs, where each epoch used data from a
256 different bootstrapped set of 1000 pixels taken from *Pixel Set A*. Here, an epoch refers to the LSTM

257 training procedure wherein each temporal data sample for the entire set of 1000 pixels is used once
258 to update the values of the network parameters.

259 [26] To investigate the informational value of different variables used as input data, we developed
260 the 4 different LSTM models indicated below. To keep track of the different models we adopt the
261 following four-part naming convention where the first part refers to the model type (LSTM or
262 SN17), the second part refers to the Pixel Set used (A or B; *Pixel Set B* will be introduced later),
263 the third part refers to the model domain (CONUS or Region), and the fourth part refers to the
264 variables used as input data (PT, PTE, 6M and 6ME). In regard to the latter, PT refers to
265 precipitation and temperature, PTE refers to precipitation and temperature plus elevation, 6M
266 refers to a set of 6 meteorological variables (precipitation, temperature, dew point temperature,
267 vapor pressure deficit, longwave radiation and shortwave radiation), and 6ME refers to the set of
268 6 meteorological variables plus elevation.

269 [27] Accordingly, the four LSTM models developed for Experiment 1 were all CONUS-wide
270 LSTMs trained on all pixels from *Pixel Set A*, as indicated below:

271 **LSTM-A-CONUS-PT**: This LSTM was trained using only precipitation and mean temperature
272 as forcing inputs; no information about local static pixel attributes (such as elevation, etc) was
273 used for development of this model.

274 **LSTM-A-CONUS-PTE**: This LSTM was trained using precipitation and mean temperature as
275 forcing inputs, and with pixel mean elevation provided at each pixel.

276 **LSTM-A-CONUS-6M**: This LSTM was trained using the set of 6 meteorological forcing
277 inputs, without being provided any information about local static pixel attributes.

278 **LSTM-A-CONUS-6ME**: This LSTM was trained using the set of 6 meteorological forcing
279 inputs, and with pixel mean elevation provided for each pixel.

280 [28] As benchmarks for comparison, we developed two SN17 models. Note that SN17 currently
281 uses only precipitation, temperature and elevation as input data.

282 **SN17-A-CONUS**: A single CONUS-wide SN17 model was calibrated to obtain a single “*best-*
283 *average*” CONUS-wide set of parameters whose values were applied simultaneously to all of
284 the pixels from *Pixel Set A*.

285 **SN17-A-PX**: The SN17 model was calibrated separately at each pixel in *Pixel Set A* resulting
286 in different parameter sets at each of the 15,000 pixels.

287 As such, the **SN17-A-CONUS** model can be thought of as representing a “*lower-benchmark*” on
288 SN17 performance at each pixel, since this model treats all pixels as having identical functional
289 characteristics, and simply applies the same input-state-output transformation algorithm to every
290 pixel regardless of its location or local static characteristics. In contrast, the **SN17-A-PX** model
291 can be thought of as representing an “*upper benchmark*” on SN17 performance at each of the
292 calibrated pixels, since the model was tuned specifically to optimize performance at those pixels.

293 **3.2.2 Experiment 2: Regional modeling of snow accumulation and melt**

294 [29] For this second experiment, we developed another set of 15,000 pixels, hereafter referred to
295 as *Pixel Set B*, by randomly selecting 3,000 pixels from each of the 5 study regions (OH, MO,
296 CRB, SN and CC). Note that these five regions represent 13.11%, 3.53%, 13.79%, 67.93% and
297 44.14% respectively of the total number of snowy pixels across the CONUS. Further, each region
298 includes a different percentage of forested and non-forested areas. As a result, *Pixel Set B* has

299 relatively dense representation of forested regions and is most sparsely representative of the
300 Missouri river basin, which is the largest of the five regions.

301 [30] Using *Pixel Set B*, we again trained the LSTM architecture at the CONUS level (a single
302 model for the entire country), after which we trained separate LSTM models for each region (5
303 separate models, one for each region). The procedure used was as follows. For each region, we
304 partitioned the corresponding 3,000 pixels into sets of 1000 each for training, validation and testing.
305 For the CONUS-wide model(s) the 1000 "training" pixels from each of the five regions were
306 grouped together to obtain 5000 pixels to be used for network training (similarly for validation and
307 testing). For each of the regional models, only the corresponding regional pixels were used for
308 network training, validation and testing.

309 [31] To initialize each CONUS-wide LSTM model (see below), we initialized the weights and
310 biases using the corresponding results obtained at the end of the 15th epoch of Experiment 1; in
311 other words, the network architectures were considered to have been "pre-trained" using the
312 information provided by *Pixel Set A*. The networks were then trained for 30 epochs, and the
313 network parameters (weights and biases) were recorded for the epoch at which the highest average
314 Kling–Gupta efficiency (KGE; *Gupta et al., 2009*) was achieved over the 5,000 validation pixels.
315 By doing so, we took advantage of the results of Experiment 1 to minimize training costs, while
316 achieving a consistent set of weights and biases for the CONUS-wide model that could be used
317 when initializing the training of the separate regional models. In this way, we took advantage of
318 the benefits of "transfer learning" (*Kratzert et al., 2018*).

319 [32] As in Experiment 1, we developed four different LSTM models at the CONUS level, trained
320 on Pixel Set B, as indicated below:

321 **LSTM-B-CONUS-PT**: This LSTM was trained using only precipitation and mean temperature
322 as forcing inputs; no information about local static pixel attributes (such as elevation, etc) was
323 used for development of this model.

324 **LSTM-B-CONUS-PTE**: This LSTM was trained using precipitation and mean temperature as
325 forcing inputs, and with pixel mean elevation provided at each pixel.

326 **LSTM-B-CONUS-6M**: This LSTM was trained using the set of 6 meteorological forcing
327 inputs, without being provided any information about local static pixel attributes.

328 **LSTM-B-CONUS-6ME**: This LSTM was trained using the set of 6 meteorological forcing
329 inputs, and with pixel mean elevation provided for each pixel.

330 [33] Similarly, for each Regional LSTM model (see below), we initialized the weights and biases
331 using the corresponding results obtained from the CONUS-wide models trained on *Pixel Set B*; in
332 other words, the regional network architectures were considered to have been "pre-trained" using
333 the information provided by the CONUS-wide model trained on *Pixel Set B*. The networks were
334 then trained for 30 epochs, and the network parameters (weights and biases) were recorded for the
335 epoch at which the highest average KGE value was achieved over the corresponding regional
336 validation pixels. This approach took advantage of the results of CONUS-wide modeling to
337 minimize training costs.

338 [34] Accordingly, we developed four different LSTM models for each Region, as indicated below:

339 **LSTM-B-Region-PT**: Each regional LSTM was trained using only precipitation and mean
340 temperature as forcing inputs; no information about local static pixel attributes (such as
341 elevation, etc.) was used for development of these models.

342 **LSTM-B-Region-PTE**: Each regional LSTM was trained using precipitation and mean
343 temperature as forcing inputs, and with pixel mean elevation provided at each pixel.

344 **LSTM-B-Region-6M**: Each regional LSTM was trained using the set of 6 meteorological
345 forcing inputs, without being provided any information about local static pixel attributes.

346 **LSTM-B-Region-6ME**: Each regional LSTM was trained using the set of 6 meteorological
347 forcing inputs, and with pixel mean elevation provided for each pixel.

348 [35] As benchmarks for comparison, we developed the following additional SN17 models:

349 **SN17-B-CONUS**: A single CONUS-wide SN17 model calibrated to obtain a single “*best-*
350 *average*” CONUS-wide set of parameters for all of the pixels from *Pixel Set B*.

351 **SN17-B-Region**: Five Regional SN17 models calibrated to obtain “*best-average*” region-wide
352 sets of parameters for the pixels in each region of *Pixel Set B*.

353 **SN17-B-PX**: The SN17 model was calibrated separately at each pixel in *Pixel Set B* resulting
354 in different parameter sets at each of the 15,000 pixels.

355 [36] For model evaluation/testing, we focused on how well the models perform on the 5,000
356 testing pixels selected from *Pixel Set B* (1000 pixels from each of the 5 regions). First, we evaluated
357 the LSTM-based models against the SN17 benchmarks when using only PTE (precipitation, mean
358 temperature and elevation) as inputs, these being the same inputs used by SN17. The goal was to
359 assess the capability of the LSTM network architecture to learn an appropriate representation of
360 snow accumulation and melt over different training phases given the same input information that
361 is available to the SN17 model. Then, we assessed which combination of inputs (PT, PTE, 6M or
362 6ME) results in the best LSTM-based CONUS-wide predictions. Finally, we examined whether
363 regional training results in better model performance than using the CONUS-wide model(s). Note
364 that in all cases, the LSTM-based models were fine-tuned on *Pixel Set B* after initializing using
365 weights and biases trained on *Pixel Set A*.

366 **3.2.3 Experiment 3: Exploring the benefits of transfer learning**

367 [37] For the third experiment, we investigated the extent to which different spatial regions can
368 share a common model structure with different parameter values through transfer learning (TL)
369 across regions. Each LSTM-B-Region model trained in Experiment 2 was applied to each of the
370 other four regions, resulting in 20 TL models for each input combination (PT, PTE, 6M or 6ME):

371 **LSTM-B-TL from Ohio**: For each of the regions MO, CRB, SN and CC, we obtain 4 TL-
372 LSTM networks, trained with different input combinations on the OH Region.

373 **LSTM-B-TL from Missouri**: For each of the regions OH, CRB, SN and CC, we obtain 4 TL-
374 LSTM networks, trained with different input combinations on the MO Region

375 **LSTM-B-TL from CRB**: For each of the regions MO, OH, SN and CC, we obtain 4 TL-LSTM
376 networks, trained with different input combinations on the CRB Region

377 **LSTM-B-TL from SN**: For each of the regions MO, CRB, OH and CC, we obtain 4 TL-LSTM
378 networks, trained with different input combinations on the SN Region

379 **LSTM-B-TL from Cascades:** For each of the regions MO, CRB, SN and OH, we obtain 4 TL-
 380 LSTM networks, trained with different input combinations on the CC Region

381 [38] The goal of this experiment was to test the extent to which a regional LSTM model structure
 382 hypothesis, imposed in the form of different kinds of regularization strategies at the input, can be
 383 transferred (extrapolated) to other locations. We benchmarked these TL-LSTM networks against
 384 the 3 models listed in Experiment 2 (*LSTM-B-Region*, *SN17-B-Region* and *SN17-B-PX*) to
 385 examine how well the information about system structure extracted from region can be transferred
 386 to another. To ensure a clean evaluation, the results were only assessed over the 5,000 testing
 387 pixels.

388 3.3 Objective Function

389 [39] The objective function used for CONUS-wide and regional model training was NSE_{avg} ,
 390 obtained by averaging the NSE values computed at each pixel that supplies training data (*Krazert*
 391 *et al., 2019b*) shown as Eqn (1):

$$392 \quad 393 \quad NSE_{avg} = \frac{1}{P} \sum_{p=1}^P \sum_{n=1}^N \frac{(\widehat{y}_n - y_n)^2}{(s(p) + \epsilon)^2} \quad (1)$$

394 where P is the number of pixels, N is the number of days per pixel, \widehat{y}_n is the prediction of
 395 pixel $n(1 \leq n \leq N)$, y_n is the observation, and $s(p)$ is the standard deviation of the SWE in
 397 pixel $p(1 \leq p \leq P)$, calculated from the training period. The value of ϵ was set to 0.1 to avoid the
 398 loss function exploding to infinity for pixels with very low SWE variance. For training the pixel-
 399 wise SN17 model we used the standard NSE shown in Eqn (2):

$$400 \quad 401 \quad NSE = 1 - \frac{\sum_{t=1}^T (\widehat{y}_n^t - y_n^t)^2}{\sum_{t=1}^T (y_n^t - \overline{y}_n)^2} \quad (2)$$

402 where \overline{y}_n is the mean of observed SWE for each day, \widehat{y}_n^t and y_n^t are the modeled and observed
 403 SWE at the training period time $t(1 \leq t \leq T)$ for a single pixel.

405 3.4 Hyperparameter and Training Details

406 [40] We **mostly** followed *Krazert et al. (2019b)* for setting the LSTM hyperparameters; 256
 407 hidden states, 1 stacked LSTM layer, a batch size of 256, a dropout rate of 0.4 and a sequentially
 408 decreased learning rate per 10 epochs from 1.0×10^{-3} to 5.0×10^{-4} then to 1.0×10^{-4} . The
 409 LSTMs were run in sequence-to-value mode, so that to predict a single daily SWE value the
 410 meteorological forcing from 242 preceding days, as well as the forcing data of the target day, were
 411 used (making the input sequences 243 time-steps long). This input sequence length follows
 412 suggestions from the land model community, where the snowy season is typically assumed to last
 413 from October 1st to May 31st resulting in a total of 243 days (*Niu and Yang 2007; Swenson and*
 414 *Lawrence 2012*). The relatively large number of hidden states (256) is believed to help circumvent
 415 the situation where the predictive performance of the LSTM is sensitive to weight initialization
 416 when using a small number of hidden state units (*Bengio, 2012*). The ADAM optimization
 417 algorithm was used for training (*Kingma and Ba, 2014*). Also, a single fixed random seed (2925)
 418 was applied to train all the LSTM networks. Our results indicated robust performance over 3

419 independent testing pixel sets (see section 4.1.3), and therefore no further hyperparameter tuning
 420 was performed.

421 [41] Note that in experiment 1 we trained the LSTM network for a total of 15 epochs, where each
 422 epoch used data from a different bootstrapped set of 1000 pixels taken from *Pixel Set A*. The results
 423 of 15th epoch were then used to initialize the training for experiment 2, in which the LSTM network
 424 was trained for a total of 30 epochs using data from 5,000 training pixels selected from *Pixel Set*
 425 *B*. The results for the epoch having a minimum averaged KGE value over 5,000 validation pixels
 426 were then used to initialize the next stage of training for the 5 regional networks. Model
 427 performance was then assessed for an independent set of 5,000 testing pixels.

428 [42] To calibrate the SN17 models, we used the Shuffled Complex Evolution (SCE) global
 429 optimization algorithm (*Duan et al., 1992*). Ten parameters were optimized, with the parameter
 430 range and model structure following *He et al. (2011a)*. A standard batch calibration procedure was
 431 employed in which all training pixels were processed simultaneously at each iteration, in contrast
 432 to LSTM training where we randomly sampled pixels to make up each training batch to achieve
 433 faster convergence (*LeCun et al., 2012*).

434 3.5 Evaluation Metrics for Assessing Model Performance

435 [43] To assess the consistency, reliability, accuracy, and precision of the models, we used several
 436 metrics, including NSE (*Nash and Sutcliffe, 1970*; Eqn 2), the three components of KGE (*Gupta*
 437 *et al., 2009*) from Eqn(3) to Eqn(6), and the scaled KGE (hereafter KGE_{ss}; *Khatami et al., 2020*;
 438 Eqn 7):

$$439 \alpha = \frac{\sigma_s}{\sigma_o} \quad (3)$$

$$440 \beta = \frac{\mu_s}{\mu_o} \quad (4)$$

$$441 \gamma = \frac{Cov_{so}}{\sigma_s \sigma_o} \quad (5)$$

$$442 KGE = 1 - \sqrt{((\gamma - 1)^2 + (\beta - 1)^2 + (\alpha - 1)^2)} \quad (6)$$

$$443 KGE_{ss} = 1 - \frac{(1-KGE)}{\sqrt{2}} \quad (7)$$

444 where σ_s and σ_o are the standard deviation, and μ_s and μ_o are the mean of the simulated and
 445 observed SWE time series respectively, and Cov_{so} is the covariance between the simulated and
 446 observed values.

449 4. Results and Discussion

450 4.1 Experiment 1: CONUS-wide modeling of snow accumulation and melt

451 [44] *Figures 2* and *3* present a statistical assessment of the potential for using the LSTM
 452 architecture to model CONUS-wide snow accumulation and melt. The results show CDFs of
 453 testing-pixel performance over 15,000 pixels from *Pixel Set A* for the four CONUS-wide LSTM
 454 models (*LSTM-A-CONUS-PT*, *-PTE*, *-6M* and *-6ME*) that use different input data sets, the lower-
 455 benchmark *SN17-A-CONUS* model, and the upper-benchmark *SN17-A-PX* model used as the bases
 456 for comparison. Note that each of these six models uses a single architecture to model snow
 457 accumulation and melt dynamics across the entire CONUS. Recall that the lower-benchmark

458 *SN17-A-CONUS* model and the four LSTM models each use a single set of CONUS-wide
459 parameters, while the *SN17-A-PX* model is individually trained to each pixel.

460 **4.1.1 Comparative overall performance of the LSTM and SN17 model architectures**

461 [45] The NSE aggregate performance results (**Figure 2**) show clearly that the LSTM architecture
462 provides better modeling of the general dynamics of snow accumulation and melt than the SN17
463 model architecture. All of the CDFs are shifted much further to the right, closer to the ideal value
464 of 1.0. With a single network architecture and set of parameters applied to the entire CONUS,
465 each of the four LSTM models (solid lines) achieves significantly better distributions of testing-
466 pixel NSE scores than the lower- and upper-benchmark SN17 models (blue and red dashed lines
467 respectively). In particular, the LSTM network architecture, with CONUS-wide sets of parameters
468 (red, orange, purple and green solid lines), provides better performance than the *SN17-A-PX* model
469 for which parameters were optimized locally at each pixel. The unavoidable conclusion is that the
470 SN17 model architecture does not adequately capture the structural nature of the input-state-output
471 transformations that express the dynamics of snow accumulation and melt.

472 **4.1.2 Ability of the LSTM and SN17 architectures to exploit information in the input data**

473 [46] Although the *NSE* metric indicates better aggregate performance of the LSTM architecture,
474 it does not provide much insight into the reasons why. Note also that the use of different time
475 periods to compute the aggregated NSE performance criterion can be informative (*Schaefli et al.,*
476 *2005; Schaefli and Gupta, 2007*). Here, we use the *KGEss* performance metric and its components
477 to provide better discrimination between the models. The top row (a to d) of subplots in **Figure 3**
478 compares the results when both model types are provided with similar input data (precipitation,
479 temperature and elevation).

480 [47] First, both the *LSTM-A-CONUS-PT* and *LSTM-A-CONUS-PTE* networks (red and orange
481 solid lines respectively) achieve significantly better *KGEss* performance than the *SN17-A-CONUS*
482 model (blue dashed line). Further, the γKGE component shows that a major reason for this is that
483 the LSTM is better able to simulate the shape and timing of snowmelt. So, even without any
484 information regarding “*local*” properties of the landscape, the *LSTM-A-CONUS-PT* (which was
485 *not* provided local elevation information) model is able to learn an input-state-output mapping that
486 is better than that encoded by the SN17 model (which *was* provided with elevation information).
487 In other words, the LSTM architecture is able to make better use of the information about snow
488 dynamics provided by the input (precipitation and temperature) data.

489 [48] Second, the *LSTM-A-CONUS-PTE* network *with* elevation information (orange solid line) is
490 clearly better than the *LSTM-A-CONUS-PT* network *without* elevation information (red solid line).
491 In particular, the use of elevation information results in a much better mass balance, as indicated
492 by the $\beta - KGE$ curve being closer to the ideal value of 1. This indicates, as might be expected,
493 that there is considerable predictive value provided by the “*local*” information about elevation.

494 [49] Third, the *LSTM-A-CONUS-PTE* network, with a single set of CONUS-wide parameters,
495 achieves almost identical *KGEss* performance to that of the *SN17-A-PX* model that was calibrated
496 individually to each pixel (note that both these models use the same physical input information).
497 This indicates that the LSTM architecture is able to successfully learn a set of parameters that
498 enables it to be confidently applied to pixels that were not used for network training.

499 [50] The bottom row (e to h) of subplots in **Figure 3** compares the results when the LSTM network
500 architecture is provided with different types of input data (red, orange, purple and green solid lines).

501 As indicated above, there is significant improvement when going from *PT* where only precipitation
502 and temperature are provided (red solid line) to *PTE* where elevation information is also provided
503 (orange solid line). However, even further improvement is achieved by the 6M network (purple
504 solid line) that is provided with additional meteorological variables. Note that only the first two of
505 these inputs (precipitation and temperature) are used by the SN17 model. So, providing the
506 network with additional meteorological information (here dew point temperature, vapor pressure
507 deficit, longwave radiation and shortwave radiation) is clearly beneficial. However, the 6ME
508 model, which is provided with the 6 meteorological variables plus elevation, shows a clear decline
509 in overall *KGE_{ss}* performance. This seems to suggest that the information provided by elevation
510 may be redundant when the meteorological information is provided (i.e., the meteorological
511 variables already encode the useful information that would otherwise be provided by elevation).

512 [51] Overall, the *KGE* metric and its components show that the *LSTM-A-CONUS-6M* model
513 provides a much better representation of water balance and range of variability (curves are shifted
514 closer to the center, where the ideal value is 1; **Figures 3g & 3f**), achieving a median *KGE_{ss}*
515 performance of 0.94 compared with the *SN17-A-PX* model (median *KGE_{ss}*=0.93). In general, all
516 of the models tend to underestimate the variability of snowmelt ($\alpha - KGE < 1$; **Figures 3b & 3g**).
517 Both the *LSTM-A-CONUS-PTE* and *LSTM-A-CONUS-6M* models provide better representations
518 of snow mass balance ($\beta - KGE$ closer to 1; **Figures 3c & 3g**) than the other 2 LSTMs. Use of
519 only precipitation and mean temperature (*LSTM-A-CONUS-PT*) results in a tendency to positive
520 bias, likely because it does not have access to humidity relevant information (vapor pressure deficit,
521 dew point temperature) and is therefore unable to learn an accurate rain-snow partitioning
522 threshold within the gating operation (*Wang et al., 2019*). Meanwhile, the *SN17-A-PX* model tends
523 to underestimate mass balance suggesting that one should perhaps consider using other objective
524 functions for pixel-wise training than NSE (or *KGE*, not shown, which results in similar
525 underestimation bias).

526 [52] In summary, the ability to exploit the information provided by a wider suite of meteorological
527 variables enables the CONUS-wide implementation of the LSTM architecture to achieve a better
528 representation of the dynamics of snow accumulation and melt, as assessed in terms of the ability
529 to match the target SWE variable. However, even when provided with the same physical inputs as
530 SN17, the LSTM architecture provides better results; such an implementation might be
531 unavoidable when only Snow Telemetry (SNOTEL) information is available.

532 **4.1.3 Evaluation on Pixel Set B**

533 [53] We next evaluated the *LSTM-A-CONUS-6M* model trained using *Pixel-Set-A* on a different
534 set of 15,000 pixels from *Pixel Set B*. **Figure 4** summarizes the spatial distributions of the 5
535 performance metrics separately for first independent sets (see other two sets in **Figure S3**) of 5,000
536 pixels from *Pixel Set B*. **Table 2** shows that, overall, the model continues to provide good predictive
537 performance on all three independent datasets, with only 31.69% and 30.22% of the pixels having
538 more than $\pm 10\%$ bias in the values of $\alpha - KGE$ and $\beta - KGE$ respectively. Further detailed
539 evaluation performed on each of the five regions (see Experiment 2) reinforced these findings (see
540 **Figure S1**). Overall, these results indicate that the CONUS-wide *LSTM-A-CONUS-6M* model
541 achieves a high degree of robustness with regard to predictive performance. As such, no further
542 tuning of the LSTM model hyperparameters was performed in the later parts of this study.

543 [54] The CDF plots related to **Figure 6** are presented in **Figure S4** of the Supplementary Materials.
544 Generally, MO and CRB have an overall better performance in terms of *KGE_{ss}* and NSE whereas

545 the two forested areas, SN and CC, perform relatively worse, with OH being in between. A similar
546 conclusion is found by examining three KGE components except that the OH shows a relatively
547 large negative bias for the standard deviation error ($\alpha - KGE$). **Table 3** summarizes the Pearson
548 correlation coefficient (γ) for the pair of SWE hydrographs within the study period. MO and CRB
549 have the two lowest average γ values for all the pairs (0.47 and 0.47 respectively) which suggests
550 that the *LSTM-A-CONUS-6ME* model trained over the entire country provides better performance
551 when the region covers a more diversified climatic regime. Moreover, the model has worse average
552 performance at forested (as opposed to non-forested) pixels, where the average KGEss skill
553 difference between the two area equals 0.015, 0.079 and 0.023 over OH, SN and CC respectively.
554 Further, the KGEss skill is only 0.55 and 0.75 for Mixed Forest and Woody Savanna pixels in the
555 SN region, suggesting the need to either construct separate local models, or to add relevant local
556 attributes to the CONUS-wide models to improve overall LSTM model performance.

557 [55] **Figure S5** and **S6** show that the CONUS-wide LSTM is able to properly simulate the seasonal
558 cycle dynamics of snow accumulation and melt. The figures show, for each region, time-series
559 comparisons of simulated and observed SWE for the *LSTM-A-CONUS-6M* model and various
560 versions of the SN17 model. Although a very large number of cases was investigated in this study,
561 the results presented here can be considered to be representative.

562 **4.2 Experiment 2: Regional modeling of snow accumulation and melt**

563 **4.2.1 Results of CONUS-wide Fine Tuning**

564 [56] Experiment 2 was conducted in stages, where the first stage was another round of CONUS-
565 wide network training. In the following discussion, we refer to the LSTM networks obtained by
566 training on *Pixel Set A* as the “pre-trained” CONUS-wide networks. Initialized from the weights
567 and bias parameters of these pre-trained networks we conducted a further stage of CONUS-wide
568 network training using *Pixel Set B* (called the “fine-tuned” CONUS-wide networks). The results
569 of this second round of network training are the *LSTM-B-CONUS-PT*, *-PTE*, *-6M* and *-6ME*
570 CONUS-wide models, as described in Section 3.2.2.

571 [57] Performance comparison of the pre-trained (using *Pixel-Set-A*) and the fine-tuned (using
572 *Pixel-Set-B*) CONUS-wide LSTM networks is shown in **Figure 5**. The results show performance
573 on the 5,000 independent testing pixels from *Pixel Set B*. Note that while, performance was already
574 quite good based on *Pixel-Set-A* training, the model skill, as measured by the median value of
575 KGEss, improves by ~ 0.08 / ~ 0.06 / ~ 0.08 for the *PT* / *PTE* / *6ME* models respectively, and by
576 only ~ 0.01 for the *6M* model. This reinforces the earlier finding that use of a full suite of
577 meteorological variables results in an efficient basis for training the LSTM network. However,
578 providing the network with additional information about elevation (*-6ME* model) does not result
579 in further improvement.

580 [58] This added value of fine-tuning is further demonstrated in **Figure 6**, which shows the change
581 in model skill from *LSTM-A-CONUS-6M* to *LSTM-B-CONUS-6M*. The left column of subplots
582 shows the geographical distribution of change in model skill (blue indicates improvement) while
583 the right column shows the corresponding performance difference CDFs individually for each of
584 the five regions. In the right column, the metric α^*KGE is defined as $1 - |1 - \alpha|$ and the metric
585 $\beta^* - KGE$ is defined as $1 - |1 - \beta|$ so as to better illustrate the change in skill. Accordingly,
586 positives values in the right column of subplots indicate improved performance of *LSTM-B-*
587 *CONUS-6M* over *LSTM-A-CONUS-6M* with respect to the corresponding metric.

588 [59] Accordingly, of the 5000 testing pixels, 58.0% have improved NSE while 57.8% have
589 improved KGEss (with 59.6%, 54.2% and 55.8% improvement for the α , β and γ components
590 respectively). More than half of the pixels show improvements for NSE and all three components
591 of KGE for the regions other than OH. In OH, as many as 60% of the pixels show a decrease in
592 KGEss skill (due to $\gamma - KGE$). This may be because *Pixel-Set-A* contains a larger number of non-
593 forested snowy pixels (77%) over the CONUS than *Pixel-Set-B* (62%). Since the CONUS-wide
594 model has to select network parameters that balance performance over both forested and non-
595 forested areas, the result seems to be improved over forested areas (which are better represented
596 by *Pixel-Set-B*) at the expense of non-forested areas.

597 **4.2.2 Regional Training of the LSTM models**

598 [60] Initialized from the weights and bias parameters of the fine-tuned CONUS-wide networks
599 we next trained a separate LSTM network for each of the 5 regions, again using *Pixel-Set-B* (we
600 refer to these as the “*fine-tuned*” regional networks). Overall, at the CONUS-level, the regional
601 tuning results in the median CDF of KGEss improving by a small amount – by 0.013, 0.012, 0.013
602 and 0.025 for the PT, PTE, 6M and 6ME models respectively (see **Figure S7** in the Supplementary
603 Materials). While the *6ME* model shows the largest improvement, its overall performance is still
604 worse than for the other models (consistent with previous results).

605 [61] In contrast with the CONUS-wide fine-tuning stage (**Figure 6**), regional fine-tuning results
606 in even more improvement of model skill across the five regions (**Figure 7**). The range of
607 improvement is from 55% (SN) to 65% (MO) for $\alpha - KGE$, from 56% (SN) to 62% (CRB) for
608 $\beta - KGE$, and from 77% (SN) to 88% (OH) for $\gamma - KGE$. Overall, 81% of the testing pixels show
609 improved NSE skill, while 64% show improved KGEss (60%, 59% and 81% for α , β and γ
610 components respectively). Meanwhile 85% (68%) of the forested pixels show greater improved
611 NSE (KGEss) skill than the CONUS-wide fine-tuning 54% (51%) over the SN region. A general
612 conclusion is that allowing the LSTM network to account for regional differences helps improve
613 predictive performance, especially over forested areas.

614 **4.2.3 Comparison with SN17 Benchmarks**

615 [62] The results reported above indicate that the best performing model is the *LSTM-B-Region-*
616 *6M* deep learning network architecture trained separately to each region. In this section, we
617 evaluate the extent to which the LSTM architecture is able to “*learn*” a better input-output mapping
618 than is encoded by the SN17 model, when both modeling strategies are provided with the *exact*
619 *same* input information (precipitation, temperature and elevation) over different phase of model
620 development. **Figure 8** summarizes the progression of performance of the LSTM architecture
621 (evaluated over the 5000 *Pixel-Set-B* testing pixels), starting with the pre-trained *LSTM-A-*
622 *CONUS-PTE*, proceeding to the fine-tuned *LSTM-B-CONUS-PTE*, and finally to the five fine-
623 tuned *LSTM-A-Region-PTE* models (here grouped together as one larger CONUS-wide model with
624 regional differentiation). As benchmarks for comparison we show the *SN17-A-CONUS* model
625 (black dashed line) and corresponding *SN17-B-CONUS* model (red dashed line), each of which
626 uses a single set of parameters to represent the entire CONUS, the *SN17-B-Region* model (blue
627 dashed line) that uses five different parameter sets (one set for each of the five regions), and an
628 “*upper-benchmark*” *SN17-B-Pixel* model (black dotted line) that is individually calibrated to each
629 of the 5000 testing pixels (thereby reflecting the best possible performance achievable at those
630 pixels by the SN17 model architecture given the available data).

631 [63] First, we notice that, as might reasonably be expected, the SN17 and LSTM models get
632 progressively better (in terms of all of the reported metrics) as we proceed from the *CONUS* to
633 *Regional* versions. However, this progressive improvement is much more significant for the SN17
634 model (see KGE_{α} – KGE and β – KGE metrics) than for the LSTM models. Further, the
635 LSTM architecture has learned a far better than representation of the snow-accumulation and melt
636 input-output mapping than is expressed by the SN17 model architecture. In terms of the NSE
637 metric, all three LSTM models (*A-CONUS*, *B-CONUS* and *B-Regional*) achieve median NSE
638 values above 0.95, while the best comparable SN17 model (*SN17-B-Regional*) achieves a median
639 NSE value of around 0.82. Note that the *SN17-B-Pixel* results, which represents a “best possible”
640 SN17 model since the model was calibrated to the testing pixels is still worse (with a median NSE
641 value of around 0.87) than all three of the LSTM models. In contrast, the KGE_{α} metric indicates
642 that the pre-trained *LSTM-A-CONUS-PTE* model is only slightly better than the *SN17-B-Region*
643 model and worse than the *SN17-B-Pixel* benchmark. Meanwhile the *LSTM-B-CONUS-PTE* and
644 *LSTM-A-Region-PTE* models have the best performance.

645 [64] Finally, it should be noted that although the improvement from *LSTM-B-CONUS-PTE* to
646 *LSTM-A-Region-PTE* is both clear and consistent, it is not very large; this indicates that a trained
647 CONUS-wide LSTM model (based on PTE data) is capable of providing almost as good
648 performance as a regionally trained one. Further this CONUS-wide LSTM is better than the
649 regionally trained SN17 model and is even better than the “perfect” SN17-B-Pixel model that was
650 calibrated to achieve best possible performance at the “testing” pixels; this latter finding is
651 consistent with the “prediction in ungauged basins” results reported by (Krazert *et al.*, 2019a;
652 Krazert *et al.*, 2019b) in the context of rainfall-runoff modeling.

653 4.2.4 Some General Remarks

654 [65] In general, the good performance of the LSTM-based models should (perhaps) not be too
655 surprising since it is likely that a much larger amount of information has been assimilated by the
656 deep learning process than was available to the developers of the SN17 model architecture. What
657 does seem remarkable is that the collective-regionally-differentiated (“fine-tuned” CONUS-wide)
658 LSTM model is not very much better than the single CONUS-wide representation, suggesting that
659 the latter *may* be capable of providing acceptably good predictions of SWE at locations that are
660 not necessarily similar, in terms of local attributes, to the conditions experienced by the model
661 during training; in other words, the conditions determining the dynamics of snow accumulation
662 and melt depend largely on meteorological and local conditions may have only marginal impact,
663 at least at the scale of the individual pixels used for this study.

664 4.3 Experiment 3: Exploring the benefits of transfer learning

665 [66] In Experiment 1, we demonstrated the ability of a CONUS-wide LSTM to make accurate and
666 robust predictions at continental scale, across different pixel sets. In Experiment 2, we showed that
667 a regionally trained LSTM also shows promising performance when tested on independent pixels
668 within the same region. Here, we explore the potential for transfer learning (TL), in which we
669 evaluate the extent to which an LSTM trained to one region can be used outside of the original
670 regional for which it was developed. This is achieved by applying the regional LSTM network
671 (*LSTM-B-Region*) trained from one region to the remaining 4 corresponding regions and
672 evaluating performance on 1,000 testing pixels selected (within that region) from Pixel Set B. The
673 evaluation results in total 20 TL evaluations for each type of LSTM (PT, PTE, 6M, 6ME) that uses
674 different input information.

675 **4.3.1 Evaluation Metric for Transfer Learning**

676 [67] To quantify the KGEss performance of each regional TL-LSTM network, we compute the
 677 area under the CDF curve integrated between 0 and 1 (i.e., positive values of KGEss). We then
 678 obtain the $\phi_{S \rightarrow T}$ TL metric by subtracting the integrated area from 1.0 as shown by Eqn (8):

679
$$\phi_{S \rightarrow T} = 1 - \int_0^1 f_{KGEss} d(KGE_{ss}) \quad (8)$$

680 [68] The symbol S refers to the source region where the TL network was developed, T refers to
 681 the target region that the network is applied to, and f_{KGEss} indicates the KGEss performance CDF
 682 of the TL network. Because KGEss performance is generally positive for all of the cases examined,
 683 we neglect area under the CDF curve corresponding to KGEss less than 0. Accordingly, the $\phi_{S \rightarrow T}$
 684 metric is bounded between 0 and 1 with larger values indicating better TL performance. Finally,
 685 the degree of transferability of each regional LSTM is evaluated as the ratio written as Eqn (9):

686
$$R_{S \rightarrow T} = \frac{\phi_{S \rightarrow T}}{\phi_T} \quad (9)$$

687 where ϕ_T refers to the metric (Eqn 8) computed for the model when trained specifically to the
 688 target region (i.e., not transferred). Accordingly, we compare the regional TL-LSTM networks
 689 against three benchmarks, including the regional LSTM model trained to the target region ($\phi_{T_{LSTM}}$),
 690 the regional SN17 model trained to the target region ($\phi_{T_{SN17-Region}}$) and the SN17 pixel model
 691 trained to the target region ($\phi_{T_{SN17-PX}}$). Thus, values of $R_{S \rightarrow T}$ larger than 1.0 indicate that the TL
 692 model is able to outperform the benchmark model, while values less than one indicate poor ability
 693 to exploit transfer learning.

694 **4.3.2 Evaluation of regional TL networks against three benchmarks**

695 [69] We first compare the TL-LSTMs against the target region LSTMs (see [Figure 9](#)). We ignore
 696 the 6ME network, because it performs worse than the PT, PTE and 6M networks while requiring
 697 more input information. Overall, we see that the *LSTM-PT* networks, which require fewer input
 698 data provide better TL performance ([Figure 9a](#)) than the PTE ([Figure 9b](#)) and 6M networks
 699 ([Figure 9c](#)), as indicated by the majority of the $R_{S \rightarrow T}$ values being close to or larger than 1.0. This
 700 suggests that the LSTM-gating operations have been able to learn a better universal representation
 701 of the processes that control the rain-snow partitioning and snowmelt dynamics, by exploiting only
 702 the information provided by precipitation and mean temperature. This finding also suggests the
 703 existence of a tradeoff between model transferability and model complexity (in the sense of the
 704 number of input variables used for training the LSTM network) ([Lute and Luce, 2017](#)). However,
 705 whether this finding is general requires further investigation and consideration of issues such as
 706 data quality and quantity ([Schoups et al., 2008](#)).

707 [70] As shown by [Figures 9b](#) and [c](#), the TL results deteriorate when elevation is included as an
 708 input for LSTM network training. In particular, the $R_{S \rightarrow T}$ metric for *LSTM-B-TL from CRB*
 709 decreases to 0.88 (6M) and 0.65 (PTE) when applied to Ohio, while conversely the *LSTM-B-TL*
 710 *from Ohio* decreases to 0.92 (6M) and 0.57 (PTE) when applied to CRB. So, the inclusion of
 711 elevation as training information tends to cause the LSTM to learn a regional representation that
 712 does not transfer well to other regions.

713 [71] Similarly, the PTE and 6M versions of the *Cascades LSTM-B-TL* do not transfer well to the
714 other four regions, and especially to the three non-forest regions (for which the $R_{S \rightarrow T}$ values are
715 all less than 0.50). This makes sense, since the Cascades is a relatively unique region where the
716 spatial coverage is relatively narrow and is located at higher latitudes, so that a representation is
717 learned that is locally-specific and therefore does not transfer well to geographical regions that are
718 not similar. However, this result may also be due to the way that we have fine-tuned the LSTM
719 network, because the 6ME results (*Figure S8*) also transfer poorly from *CRB* and *SN* to *OH* and
720 *MO*. Because we have allowed all of the weights and biases to be tunable at each level of network
721 training, the regional CC networks for PTE and 6M have likely forgotten some of the general
722 learning achieved through CONUS-level training. It is possible that freezing some of the weight
723 and biases during regional training may help to address the reasons for poor network transferability
724 (*Ma et al., 2021*).

725 [72] Next, we compare the TL-LSTMs to the target region SN17 benchmarks (SN17-Regional
726 and SN17-PX). We see that about 80% (*Figure 9d*), and more than half (55%; *Figure 9g*) of the
727 TL-LSTMs that used only precipitation and mean temperature as inputs outperform (indicated by
728 the blue-green color) the corresponding target region SN17-Regional and SN17-PX models. When
729 using all 6 meteorological inputs (6M) this success rate decreases to only 64% (*Figure 9f*) and
730 52% (*Figure 9i*) against the target region SN17-Regional and SN17-PX models respectively.
731 Although the TL-LSTM using PTE use the exact same type of input information as SN17, its
732 transferability shows a further decrease to 52% and 36%. So, although the LSTM may not be fully
733 exploiting the information provided by the elevation data, LSTMs trained for other regions are still
734 able (to a certain extent) to outperform the regionally or pixel-trained SN17 models. This suggests
735 that future investigations may focus on how to improve the SN17 model by either incorporating
736 more meteorological variables, or by enhancing the parameterized process representations within
737 the model.

738 [73] Finally, we note that the LSTM architecture exhibits better regional transferability than the
739 SN17 model structure (*Figure S9*). This points to a fundamental difference between what is
740 achieved when training an LSTM network as opposed to calibrating the SN17 model, where the
741 former corresponds more closely to a structure learning problem, while the latter is restricted to
742 only parameter learning given a predefined model structure.

743 **4.3.3 Remarks on spatial proximity assumption for region delineation**

744 [74] Finally, we note that the success of network transferability seems to be related to the spatial
745 proximity of the source and target regions. From *Figure 9*, we see that TL networks tend to transfer
746 well only to the nearest adjacent regions. For example, the TL networks that use only precipitation
747 and temperature (PT in *Figure 9a*), transfer well from *MO* to *OH* and *CRB*, and from *SN* to *CRB*
748 and *CC*. As an exception, the same PT network structure transfers well from *CC* to *CRB* even
749 though they are not geographically adjacent to each other. In general, however, one might
750 speculate that the traditional method for region delineation may not be optimal from the point of
751 view of knowledge transferability. Future study could focus on the use of other approaches for
752 grouping pixels, based on important climatologic characteristics such as aridity, seasonality and
753 fraction of precipitation falling as snow (*Knoben et al., 2018*), and seasonal precipitation and
754 temperature patterns (*Beck et al., 2018*), or by data-based clustering of pixels based on patterns
755 within the available data.

756 5. Conclusion, Remarks and Outlook

757 5.1 Conclusions

758 [75] In this study we have investigated the potential for continental-scale LSTM-based modeling
759 of snow accumulation and melt dynamics at the 4-km pixel scale over the CONUS. We have
760 further investigated whether regional differences, based on geographical proximity, can be
761 exploited to result in improved model performance. We followed a hierarchical training strategy
762 in which a general LSTM architecture was first learned by assuming that a single network could
763 represent SWE dynamics across the entire CONUS, followed by regional fine-tuning. We also
764 investigated the benefits of using different kinds of input information, beyond that required by the
765 SN17 model used by the US National Weather Service.

766 [76] Overall, our results indicate that a single LSTM network, trained using data sampled from
767 across the entire CONUS can provide remarkably good performance, as assessed via a variety of
768 metrics, and that further regional-scale fine-tuning of the network results in only marginal
769 improvement. Of particular relevance to future attempts to improve process-based representations
770 (e.g., to improve the structure of SN17) is that the most accurate and robust performance is
771 achieved when the network can access a variety of meteorological information (precipitation,
772 temperature, dew point temperature, vapor pressure deficit, longwave radiation and shortwave
773 radiation), indicating that precipitation, temperature and local elevation are not, by themselves,
774 sufficiently informative to model the variability of snow dynamics at the continental scale. Further,
775 when this range of meteorological information is provided to the network, the local information
776 provided by elevation becomes redundant.

777 [77] Comparison of the *LSTM-PTE* network with the physical-conceptual temperature-index-
778 based SN17 model (where both are provided the same input information) indicates that the gating-
779 operation and cell-states architecture of the LSTM enables it to learn a better representation of
780 snow accumulation and melt dynamics than is encoded by SN17, and that by doing so a single
781 CONUS-wide LSTM can significantly outperform an implementation of SN17 that is locally
782 calibrated to each pixel. This result continues to hold even when regionally-trained LSTMs are
783 tested for regional transferability, suggesting considerable potential for improving physical-based
784 representations to be applied CONUS-wide at the pixel resolution. In this context, LSTM-based
785 modeling can serve as a valuable data compression tool that can assist the process of scientific
786 hypothesis testing (*Nearing et al., 2020*), by providing insights regarding what kinds of
787 information may be missing from existing process-based representations.

788 [78] Of course, the data-intensive nature of LSTM-based modeling poses a potential barrier to the
789 application of such techniques to data-scarce parts of the world where real-world meteorological
790 forcing and SWE data are not widely available or have only limited temporal coverage. However,
791 one reason for our sequential experimental design (proceeding from generic/global to
792 specific/regional) was to explore the extent to which the use of a “*pre-trained*” LSTM network
793 might be a reasonable way to circumvent the need for large amount of “*local*” training data (see
794 also *Krazert et al., 2018*). Our results indicate that such a strategy may indeed be viable, and future
795 work should continue to explore to what specific/local extent this strategy can be pursued. In
796 particular, it could be useful to investigate the smallest homogenous-local areal extents that can be
797 differentiated while continuing to realize robust performance improvements. In this regard, studies
798 will also need to be done regarding the minimum number of pixels for which data must be provided
799 to efficiently achieve stable versions of trained CONUS-wide, Regional, and Local LSTM

800 networks, and to assess what factors must be considered when designing a robust stratified
801 sampling strategy for selecting representative pixels to ensure maximally informative data sets for
802 training, evaluation and testing. This latter will need to consider snow-process-relevant diversity
803 in terms of local ancillary variables related to various properties such as topographic and vegetation
804 (*Broxton et al., 2020*).

805 **5.2 Remarks on Model Benchmarks**

806 [79] Here, we have demonstrated only that a single ML algorithm (LSTM) can provide better
807 performance than a single physical-conceptual temperature-index-based algorithm (SN17). While
808 this is a good start, it clearly leaves many questions unasked and unanswered. In particular, we
809 have not yet conducted a comparison with a variety of physically/process-based models – to
810 cleanly perform such a comparison is nontrivial (*Krazert et al., 2019b; Lee et al., 2021*) since
811 different models may use different input information. However, this is certainly something that
812 should be explored in future work, and the potential for gaining deeper insights into the relative
813 strengths of data-based and physics-based approaches is high.

814 [80] We note that a problem when comparing “physically-based” models against data-based ones
815 is that the former is typically constrained by conservation principles to limit the amount of SWE
816 accumulation in a day to be less than or equal to the incoming precipitation. Precipitation
817 undercatch encoded in the data, can be a source of bias that affects the comparison. Under such
818 circumstances, a physically-based model can be expected to consistently simulate lower values for
819 snow accumulation, whereas a data-based approach that is restricted by mass balance constraints
820 may be able to produce a better quality simulation (*Hoedt et al., 2021*). In this regard, when the
821 underlying data used is not internally consistent and adequate data preprocessing does not occur
822 to remove biases from the data, data-based methods can have a real advantage.

823 **5.3 Outlook**

824 [81] We expect that LSTM-based modeling of snow dynamics can be used to learn a universal
825 model structure by leveraging the commonalities of meteorological data at various spatial locations
826 and resolutions, thereby providing benefits in terms of hydrological modeling for data-scarce
827 regions (*Ma et al., 2021*). Our study suggests that our LSTM-based strategy has the potential to
828 be expanded to the development of continental and even global-scale systems for forecasting snow
829 dynamics. In such systems, uncertainty quantification can be achieved either by applying Monte
830 Carlo dropout (*Fang et al., 2020; Klotz et al., 2021*) or the use of multiple ML-based algorithms
831 (*Fleming and Goodbody, 2019*). Given the large amount of data that is potentially available, further
832 rigorous testing of the LSTM-based approach at pixel-scale resolution should be performed in both
833 space and time (*Gupta et al., 2014*) with an emphasis on simulation performance with regard to
834 various snow signatures including April 1st SWE and snow residence time (*Lute and Luce, 2017;*
835 *Zeng et al., 2018*).

836 [82] Finally, physical explainability of ML-based results is a central contemporary challenge, one
837 that is key to widespread acceptance of Artificial Intelligence (AI). So far, the success of ML has
838 not been translated into significantly improved knowledge of the processes underlying snow
839 dynamics. More efforts should be made to tackling this issue in a hydrologic context (*Fleming et*
840 *al., 2021*). In our view, this can be advanced by symbiotic integration of physically-based and
841 data-based models. Recent attempts have included replacing internal process equations with
842 networks that have the ability to learn from data (*Bennett and Nijssen, 2021*), the embedding of
843 physically-based representations into ML networks (*Jiang et al., 2020*), and the imposition of mass

844 balance constraints into ML (*Hoedt et al., 2021; Nearing et al., 2021*). Another potential approach
845 is to use symbolic regression to facilitate the development of hybrid modeling systems that can
846 learn “*physically understandable*” process representations (*Udrescu and Tegmark, 2020*) while
847 adhering to the principle of parsimony (Occam's Razor; see discussion by *Weijs and Ruddell, 2020*).
848 One of the directions that we intend to pursue is to automate the search for physically-consistent
849 parameter transfer functions by a process of learning from large data sets (*Klotz et al., 2017; Feigl*
850 *et al., 2020; Gharari et al., 2021*).

851 **Acknowledgments, Samples, and Data**

- 852 • This work was partially supported by grants NA18OAR4590397 from the National
853 Oceanic and Atmospheric Administration (NOAA) OAR's OWAQ. The second author
854 acknowledges partial support by the Australian Centre of Excellence for Climate
855 System Science (CE110001028).
- 856 • The authors thank Sungwook Wi and Tirthankar Roy for providing the SNOW17 code
857 and Patrick Broxton for the discussion regarding the data used.
- 858 • The authors would also like to thank Andrew Bennett, Luis De La Fuente and
859 Mohammad Reza Ehsani for reading and commenting on the manuscript.
- 860 • The PRISM daily 4-km temperature and precipitation data are available at
861 <http://www.prism.oregonstate.edu>. The NLDAS-2 data are available online
862 (<http://www.emc.ncep.noaa.gov/mmb/nldas/>). The University of Arizona snow data
863 are available at the NSIDC data center (doi: 10.5067/0GGPB220EX6A).

References:

- Anderson, E.A., 1973. *National Weather Service river forecast system: Snow accumulation and ablation model* (Vol. 17). US Department of Commerce, National Oceanic and Atmospheric Administration, National Weather Service.
- Anderson, E.A., 2006. Snow accumulation and ablation model–SNOW-17. *US National Weather Service, Silver Spring, MD, 61*.
- Arevalo, J., Welty, J., Fan, Y. and Zeng, X., 2021. Implementation of Snowpack Treatment in the CPC Water Balance Model and Its Impact on Drought Assessment. *Journal of Hydrometeorology*. <https://doi.org/10.1175/JHM-D-20-0201.1>
- Bales, R.C., Molotch, N.P., Painter, T.H., Dettinger, M.D., Rice, R. and Dozier, J., 2006. Mountain hydrology of the western United States. *Water Resources Research*, 42(8). <https://doi.org/10.1029/2005WR004387>
- Barrett, A.P., 2003. *National operational hydrologic remote sensing center snow data assimilation system (SNODAS) products at NSIDC* (p. 19). Boulder, CO: National Snow and Ice Data Center, Cooperative Institute for Research in Environmental Sciences.
- Bartelt, P. and Lehning, M., 2002. A physical SNOWPACK model for the Swiss avalanche warning: Part I: numerical model. *Cold Regions Science and Technology*, 35(3), pp.123-145. [https://doi.org/10.1016/S0165-232X\(02\)00074-5](https://doi.org/10.1016/S0165-232X(02)00074-5)
- Beck, H.E., Zimmermann, N.E., McVicar, T.R., Vergopolan, N., Berg, A. and Wood, E.F., 2018. Present and future Köppen-Geiger climate classification maps at 1-km resolution. *Scientific data*, 5(1), pp.1-12. <https://doi.org/10.1038/sdata.2018.214>
- Bengio, Y., 2012. Practical recommendations for gradient-based training of deep architectures. In *Neural networks: Tricks of the trade* (pp. 437-478). Springer, Berlin, Heidelberg. https://doi.org/10.1007/978-3-642-35289-8_26
- Bennett, A. and Nijssen, B., 2021. Deep learned process parameterizations provide better representations of turbulent heat fluxes in hydrologic models. *Water Resources Research*, 57(5), p.e2020WR029328. <https://doi.org/10.1029/2020WR029328>
- Boisvenue, C. and Running, S.W., 2006. Impacts of climate change on natural forest productivity—evidence since the middle of the 20th century. *Global Change Biology*, 12(5), pp.862-882. <https://doi.org/10.1111/j.1365-2486.2006.01134.x>
- Broxton, P.D., Dawson, N. and Zeng, X., 2016. Linking snowfall and snow accumulation to generate spatial maps of SWE and snow depth. *Earth and Space Science*, 3(6), pp.246-256. <https://doi.org/10.1002/2016EA000174>
- Broxton, P.D., van Leeuwen, W.J. and Biederman, J.A., 2020. Forest cover and topography regulate the thin, ephemeral snowpacks of the semiarid Southwest United States. *Ecohydrology*, 13(4), p.e2202. <https://doi.org/10.1002/eco.2202>
- Broxton, P.D., van Leeuwen, W. and Biederman, J.A., 2017, December. SWANN: The Snow Water Artificial Neural Network Modelling System. In *AGU Fall Meeting Abstracts* (Vol. 2017, pp. C43B-01).

- Broxton, P.D., Zeng, X. and Dawson, N., 2016. Why do global reanalyses and land data assimilation products underestimate snow water equivalent?. *Journal of Hydrometeorology*, 17(11), pp.2743-2761. <https://doi.org/10.1175/JHM-D-16-0056.1>
- Broxton, P.D., Zeng, X., Sulla-Menashe, D. and Troch, P.A., 2014. A global land cover climatology using MODIS data. *Journal of Applied Meteorology and Climatology*, 53(6), pp.1593-1605. <https://doi.org/10.1175/JAMC-D-13-0270.1>
- Brun, E., David, P., Sudul, M. and Brunot, G., 1992. A numerical model to simulate snow-cover stratigraphy for operational avalanche forecasting. *Journal of Glaciology*, 38(128), pp.13-22. <https://doi.org/10.3189/S0022143000009552>
- Buckingham, D., Skalka, C. and Bongard, J., 2015. Inductive machine learning for improved estimation of catchment-scale snow water equivalent. *Journal of Hydrology*, 524, pp.311-325. <https://doi.org/10.1016/j.jhydrol.2015.02.042>
- Chaney, N.W., Metcalfe, P. and Wood, E.F., 2016. HydroBlocks: a field-scale resolving land surface model for application over continental extents. *Hydrological Processes*, 30(20), pp.3543-3559 <https://doi.org/10.1002/hyp.10891>
- Cho, E. and Jacobs, J.M., 2020. Extreme Value Snow Water Equivalent and Snowmelt for Infrastructure Design over the Contiguous United States. *Water Resources Research*, 56(10), p.e2020WR028126. <https://doi.org/10.1029/2020WR028126>
- Cho, E., Jacobs, J.M. and Vuyovich, C.M., 2020. The value of long-term (40 years) airborne gamma radiation SWE record for evaluating three observation-based gridded SWE data sets by seasonal snow and land cover classifications. *Water resources research*, 56(1). <https://doi.org/10.1029/2019WR025813>
- Christensen, N.S., Wood, A.W., Voisin, N., Lettenmaier, D.P. and Palmer, R.N., 2004. The effects of climate change on the hydrology and water resources of the Colorado River basin. *Climatic change*, 62(1), pp.337-363. <https://doi.org/10.1023/B:CLIM.0000013684.13621.1f>
- Clark, M.P., Kavetski, D. and Fenicia, F., 2011. Pursuing the method of multiple working hypotheses for hydrological modeling. *Water Resources Research*, 47(9). <https://doi.org/10.1029/2010WR009827>
- Clark, M.P., Schaefli, B., Schymanski, S.J., Samaniego, L., Luce, C.H., Jackson, B.M., Freer, J.E., Arnold, J.R., Moore, R.D., Istanbuloglu, E. and Ceola, S., 2016. Improving the theoretical underpinnings of process-based hydrologic models. *Water Resources Research*, 52(3), pp.2350-2365. <https://doi.org/10.1002/2015WR017910>
- Czyzowska-Wisniewski, E.H., van Leeuwen, W.J., Hirschboeck, K.K., Marsh, S.E. and Wisniewski, W.T., 2015. Fractional snow cover estimation in complex alpine-forested environments using an artificial neural network. *Remote Sensing of Environment*, 156, pp.403-417. <https://doi.org/10.1016/j.rse.2014.09.026>
- Daly, C., Neilson, R.P. and Phillips, D.L., 1994. A statistical-topographic model for mapping climatological precipitation over mountainous terrain. *Journal of Applied Meteorology and Climatology*, 33(2), pp.140-158. [https://doi.org/10.1175/1520-0450\(1994\)033<0140:ASTMFM>2.0.CO;2](https://doi.org/10.1175/1520-0450(1994)033<0140:ASTMFM>2.0.CO;2)

- Dawson, N., Broxton, P. and Zeng, X., 2018. Evaluation of remotely sensed snow water equivalent and snow cover extent over the contiguous United States. *Journal of Hydrometeorology*, 19(11), pp.1777-1791. <https://doi.org/10.1175/JHM-D-18-0007.1>
- Deems, J.S., Painter, T.H., Barsugli, J.J., Belnap, J. and Udall, B., 2013. Combined impacts of current and future dust deposition and regional warming on Colorado River Basin snow dynamics and hydrology. *Hydrology and Earth System Sciences*, 17(11), pp.4401-4413. <https://doi.org/10.5194/hess-17-4401-2013>
- Duan, Q., Sorooshian, S. and Gupta, V., 1992. Effective and efficient global optimization for conceptual rainfall-runoff models. *Water resources research*, 28(4), pp.1015-1031. <https://doi.org/10.1029/91WR02985>
- Ehsani, M.R., Behrangi, A., Adhikari, A., Song, Y., Huffman, G.J., Adler, R.F., Bolvin, D.T. and Nelkin, E.J., 2021. Assessment of the Advanced Very High-Resolution Radiometer (AVHRR) for Snowfall Retrieval in High Latitudes Using CloudSat and Machine Learning. *Journal of Hydrometeorology*. <https://doi.org/10.1175/JHM-D-20-0240.1>
- Fang, K., Kifer, D., Lawson, K. and Shen, C., 2020. Evaluating the potential and challenges of an uncertainty quantification method for long short-term memory models for soil moisture predictions. *Water Resources Research*, 56(12), p.e2020WR028095. <https://doi.org/10.1029/2020WR028095>
- Feigl, M., Herrnegger, M., Klotz, D. and Schulz, K., 2020. Function Space Optimization: A symbolic regression method for estimating parameter transfer functions for hydrological models. *Water resources research*, 56(10), p.e2020WR027385. <https://doi.org/10.1029/2020WR027385>
- Fleming, S.W. and Goodbody, A.G., 2019. A machine learning metasystem for robust probabilistic nonlinear regression-based forecasting of seasonal water availability in the US West. *IEEE Access*, 7, pp.119943-119964. <https://doi.org/10.1109/ACCESS.2019.2936989>
- Fleming, S.W., Vesselinov, V.V. and Goodbody, A.G., 2021. Augmenting geophysical interpretation of data-driven operational water supply forecast modeling for a western US river using a hybrid machine learning approach. *Journal of Hydrology*, 597, p.126327. <https://doi.org/10.1016/j.jhydrol.2021.126327>
- Ford, C.M., Kendall, A.D. and Hyndman, D.W., 2020. Effects of shifting snowmelt regimes on the hydrology of non-alpine temperate landscapes. *Journal of Hydrology*, 590, p.125517. <https://doi.org/10.1016/j.jhydrol.2020.125517>
- Garvelmann, J., Pohl, S. and Weiler, M., 2015. Spatio-temporal controls of snowmelt and runoff generation during rain-on-snow events in a mid-latitude mountain catchment. *Hydrological Processes*, 29(17), pp.3649-3664. <https://doi.org/10.1002/hyp.10460>
- Gharaei-Manesh, S., Fathzadeh, A. and Taghizadeh-Mehrjardi, R., 2016. Comparison of artificial neural network and decision tree models in estimating spatial distribution of snow depth in a semi-arid region of Iran. *Cold Regions Science and Technology*, 122, pp.26-35. <https://doi.org/10.1016/j.coldregions.2015.11.004>
- Gharari, S., Gupta, H.V., Clark, M.P., Hrachowitz, M., Fenicia, F., Matgen, P. and Savenije, H.H., Understanding the Information Content in the Hierarchy of Model Development Decisions:

Learning from data. *Water Resources Research*, p.e2020WR027948. <https://doi.org/10.1029/2020WR027948>

Gong, W., Gupta, H.V., Yang, D., Sricharan, K. and Hero III, A.O., 2013. Estimating epistemic and aleatory uncertainties during hydrologic modeling: An information theoretic approach. *Water resources research*, 49(4), pp.2253-2273. <https://doi.org/10.1002/wrcr.20161>

Gupta, H.V. and Nearing, G.S., 2014. Debates—The future of hydrological sciences: A (common) path forward? Using models and data to learn: A systems theoretic perspective on the future of hydrological science. *Water Resources Research*, 50(6), pp.5351-5359. <https://doi.org/10.1002/2013WR015096>

Gupta, H.V., Clark, M.P., Vrugt, J.A., Abramowitz, G. and Ye, M., 2012. Towards a comprehensive assessment of model structural adequacy. *Water Resources Research*, 48(8). <https://doi.org/10.1029/2011WR011044>

Gupta, H.V., Kling, H., Yilmaz, K.K. and Martinez, G.F., 2009. Decomposition of the mean squared error and NSE performance criteria: Implications for improving hydrological modelling. *Journal of hydrology*, 377(1-2), pp.80-91. <https://doi.org/10.1016/j.jhydrol.2009.08.003>

Gupta, H.V., Perrin, C., Blöschl, G., Montanari, A., Kumar, R., Clark, M. and Andréassian, V., 2014. Large-sample hydrology: a need to balance depth with breadth. *Hydrology and Earth System Sciences*, 18(2), pp.463-477. <https://doi.org/10.5194/hess-18-463-2014>

Gupta, H.V., Wagener, T. and Liu, Y., 2008. Reconciling theory with observations: elements of a diagnostic approach to model evaluation. *Hydrological Processes: An International Journal*, 22(18), pp.3802-3813. <https://doi.org/10.1002/hyp.6989>

He, M., Hogue, T.S., Franz, K.J., Margulis, S.A. and Vrugt, J.A., 2011a. Characterizing parameter sensitivity and uncertainty for a snow model across hydroclimatic regimes. *Advances in Water Resources*, 34(1), pp.114-127. <https://doi.org/10.1016/j.advwatres.2010.10.002>

He, M., Hogue, T.S., Franz, K.J., Margulis, S.A. and Vrugt, J.A., 2011b. Corruption of parameter behavior and regionalization by model and forcing data errors: A Bayesian example using the SNOW17 model. *Water Resources Research*, 47(7). <https://doi.org/10.1029/2010WR009753>

Henn, B., Newman, A.J., Livneh, B., Daly, C. and Lundquist, J.D., 2018. An assessment of differences in gridded precipitation datasets in complex terrain. *Journal of hydrology*, 556, pp.1205-1219. <https://doi.org/10.1016/j.jhydrol.2017.03.008>

Hochreiter, S. and Schmidhuber, J., 1997. Long short-term memory. *Neural computation*, 9(8), pp.1735-1780. <https://doi.org/10.1162/neco.1997.9.8.1735>

Hoedt, P.J., Kratzert, F., Klotz, D., Halmich, C., Holzleitner, M., Nearing, G., Hochreiter, S. and Klambauer, G., 2021. MC-LSTM: Mass-Conserving LSTM. *arXiv preprint arXiv:2101.05186*.

Hrachowitz, M., Savenije, H.H.G., Blöschl, G., McDonnell, J.J., Sivapalan, M., Pomeroy, J.W., Arheimer, B., Blume, T., Clark, M.P., Ehret, U. and Fenicia, F., 2013. A decade of Predictions in Ungauged Basins (PUB)—a review. *Hydrological sciences journal*, 58(6), pp.1198-1255. <https://doi.org/10.1080/02626667.2013.803183>

Huo, X., Gupta, H., Niu, G.Y., Gong, W. and Duan, Q., 2019. Parameter sensitivity analysis focomputationally intensive spatially distributed dynamical environmental systems

- models. *Journal of Advances in Modeling Earth Systems*, 11(9), pp.2896-2909. <https://doi.org/10.1029/2018MS001573>
- Jarvis, A., 2008. Hole-field seamless SRTM data, International Centre for Tropical Agriculture (CIAT). <http://srtm.csi.cgiar.org>
- Jiang, S., Zheng, Y. and Solomatine, D., 2020. Improving AI system awareness of geoscience knowledge: symbiotic integration of physical approaches and deep learning. *Geophysical Research Letters*, 47(13), p.e2020GL088229. <https://doi.org/10.1029/2020GL088229>
- Jin, J., Gao, X., Sorooshian, S., Yang, Z.L., Bales, R., Dickinson, R.E., Sun, S.F. and Wu, G.X., 1999. One-dimensional snow water and energy balance model for vegetated surfaces. *Hydrological Processes*, 13(14-15), pp.2467-2482. [https://doi.org/10.1002/\(SICI\)1099-1085\(199910\)13:14/15<2467::AID-HYP861>3.0.CO;2-J](https://doi.org/10.1002/(SICI)1099-1085(199910)13:14/15<2467::AID-HYP861>3.0.CO;2-J)
- Khatami, S., Peterson, T.J., Peel, M.C. and Western, A., 2020. Evaluating catchment models as multiple working hypotheses: on the role of error metrics, parameter sampling, model structure, and data information content. *arXiv preprint arXiv:2009.00729*.
- Kingma, D.P. and Ba, J., 2014. Adam: A method for stochastic optimization. *arXiv preprint arXiv:1412.6980*.
- Klotz, D., Herrnegger, M. and Schulz, K., 2017. Symbolic regression for the estimation of transfer functions of hydrological models. *Water Resources Research*, 53(11), pp.9402-9423. <https://doi.org/10.1002/2017WR021253>
- Klotz, D., Kratzert, F., Gauch, M., Keefe Sampson, A., Brandstetter, J., Klambauer, G., Hochreiter, S. and Nearing, G., 2021. Uncertainty Estimation with Deep Learning for Rainfall–Runoff Modelling. *Hydrology and Earth System Sciences Discussions*, pp.1-32. <https://doi.org/10.5194/hess-2021-154>
- Knoben, W.J., Woods, R.A. and Freer, J.E., 2018. A quantitative hydrological climate classification evaluated with independent streamflow data. *Water Resources Research*, 54(7), pp.5088-5109. <https://doi.org/10.1029/2018WR022913>
- Kratzert, F., Klotz, D., Brenner, C., Schulz, K. and Herrnegger, M., 2018. Rainfall–runoff modelling using long short-term memory (LSTM) networks. *Hydrology and Earth System Sciences*, 22(11), pp.6005-6022. <https://doi.org/10.5194/hess-22-6005-2018>
- Kratzert, F., Klotz, D., Herrnegger, M., Sampson, A.K., Hochreiter, S. and Nearing, G.S., 2019a. Toward improved predictions in ungauged basins: Exploiting the power of machine learning. *Water Resources Research*, 55(12), pp.11344-11354. <https://doi.org/10.1029/2019WR026065>
- Kratzert, F., Klotz, D., Shalev, G., Klambauer, G., Hochreiter, S. and Nearing, G., 2019b. Towards learning universal, regional, and local hydrological behaviors via machine learning applied to large-sample datasets. *Hydrology and Earth System Sciences*, 23(12), pp.5089-5110. <https://doi.org/10.5194/hess-23-5089-2019>
- Kuter, S., 2021. Completing the machine learning saga in fractional snow cover estimation from MODIS Terra reflectance data: Random forests versus support vector regression. *Remote Sensing of Environment*, 255, p.112294 <https://doi.org/10.1016/j.rse.2021.112294>

- LeCun, Y.A., Bottou, L., Orr, G.B. and Müller, K.R., 2012. Efficient backprop. In *Neural networks: Tricks of the trade* (pp. 9-48). Springer, Berlin, Heidelberg. https://doi.org/10.1007/978-3-642-35289-8_3
- Lees, T., Buechel, M., Anderson, B., Slater, L., Reece, S., Coxon, G. and Dadson, S.J., 2021. Benchmarking Data-Driven Rainfall-Runoff Models in Great Britain: A comparison of LSTM-based models with four lumped conceptual models. *Hydrology and Earth System Sciences Discussions*, pp.1-41. <https://doi.org/10.5194/hess-2021-127>
- Liang, X., Lettenmaier, D.P., Wood, E.F. and Burges, S.J., 1994. A simple hydrologically based model of land surface water and energy fluxes for general circulation models. *Journal of Geophysical Research: Atmospheres*, 99(D7), pp.14415-14428. <https://doi.org/10.1029/94JD00483>
- Lute, A.C. and Luce, C.H., 2017. Are model transferability and complexity antithetical? Insights from validation of a variable-complexity empirical snow model in space and time. *Water Resources Research*, 53(11), pp.8825-8850. <https://doi.org/10.1002/2017WR020752>
- Ma, K., Feng, D., Lawson, K., Tsai, W.P., Liang, C., Huang, X., Sharma, A. and Shen, C., 2021. Transferring Hydrologic Data Across Continents—Leveraging Data-Rich Regions to Improve Hydrologic Prediction in Data-Sparse Regions. *Water Resources Research*, 57(5), p.e2020WR028600. <https://doi.org/10.1029/2020WR028600>
- Mankin, J.S., Viviroli, D., Singh, D., Hoekstra, A.Y. and Diffenbaugh, N.S., 2015. The potential for snow to supply human water demand in the present and future. *Environmental Research Letters*, 10(11), p.114016. <https://doi.org/10.1088/1748-9326/10/11/114016>
- Marks, D., Domingo, J., Susong, D., Link, T. and Garen, D., 1999. A spatially distributed energy balance snowmelt model for application in mountain basins. *Hydrological processes*, 13(12-13), pp.1935-1959. [https://doi.org/10.1002/\(SICI\)1099-1085\(199909\)13:12/13<1935::AID_HYP868>3.0.CO;2-C](https://doi.org/10.1002/(SICI)1099-1085(199909)13:12/13<1935::AID_HYP868>3.0.CO;2-C)
- Mote, P.W., 2006. Climate-driven variability and trends in mountain snowpack in western North America. *Journal of Climate*, 19(23), pp.6209-6220. <https://doi.org/10.1175/JCLI3971.1>
- Musselman, K.N., Addor, N., Vano, J.A. and Molotch, N.P., 2021. Winter melt trends portend widespread declines in snow water resources. *Nature Climate Change*, pp.1-7. <https://doi.org/10.1038/s41558-021-01014-9>
- Musselman, K.N., Lehner, F., Ikeda, K., Clark, M.P., Prein, A.F., Liu, C., Barlage, M. and Rasmussen, R., 2018. Projected increases and shifts in rain-on-snow flood risk over western North America. *Nature Climate Change*, 8(9), pp.808-812. <https://doi.org/10.1038/s41558-018-0236-4>
- Nash, J.E. and Sutcliffe, J.V., 1970. River flow forecasting through conceptual models part I—A discussion of principles. *Journal of hydrology*, 10(3), pp.282-290. [https://doi.org/10.1016/0022-1694\(70\)90255-6](https://doi.org/10.1016/0022-1694(70)90255-6)
- Nearing, G.S., Kratzert, F., Sampson, A.K., Pelissier, C.S., Klotz, D., Frame, J.M., Prieto, C. and Gupta, H.V., 2021. What role does hydrological science play in the age of machine learning?. *Water Resources Research*, 57(3), p.e2020WR028091. <https://doi.org/10.1029/2020WR028091>

- Nearing, G.S., Ruddell, B.L., Bennett, A.R., Prieto, C. and Gupta, H.V., 2020. Does information theory provide a new paradigm for earth science? Hypothesis testing. *Water Resources Research*, 56(2). <https://doi.org/10.1029/2019WR024918>
- Nijssen, B., O'Donnell, G.M., Hamlet, A.F. and Lettenmaier, D.P., 2001. Hydrologic sensitivity of global rivers to climate change. *Climatic change*, 50(1), pp.143-175. <https://doi.org/10.1023/A:1010616428763>
- Niu, G.Y., Yang, Z.L., Mitchell, K.E., Chen, F., Ek, M.B., Barlage, M., Kumar, A., Manning, K., Niyogi, D., Rosero, E. and Tewari, M., 2011. The community Noah land surface model with multiparameterization options (Noah-MP): 1. Model description and evaluation with local-scale measurements. *Journal of Geophysical Research: Atmospheres*, 116(D12). <https://doi.org/10.1029/2010JD015139>
- Ntokas, K.F., Odry, J., Boucher, M.A. and Garnaud, C., 2021. Investigating ANN architectures and training to estimate snow water equivalent from snow depth. *Hydrology and Earth System Sciences*, 25(6), pp.3017-3040. <https://doi.org/10.5194/hess-25-3017-2021>
- Odry, J., Boucher, M.A., Cantet, P., Lachance-Cloutier, S., Turcotte, R. and St-Louis, P.Y., 2020. Using artificial neural networks to estimate snow water equivalent from snow depth. *Canadian Water Resources Journal/Revue canadienne des ressources hydriques*, 45(3), pp.252-268. <https://doi.org/10.1080/07011784.2020.1796817>
- Pohl, S., Marsh, P. and Liston, G.E., 2006. Spatial-temporal variability in turbulent fluxes during spring snowmelt. *Arctic, Antarctic, and Alpine Research*, 38(1), pp.136-146. [https://doi.org/10.1657/1523-0430\(2006\)038\[0136:SVITFD\]2.0.CO;2](https://doi.org/10.1657/1523-0430(2006)038[0136:SVITFD]2.0.CO;2)
- Pokhrel, P., Gupta, H.V. and Wagener, T., 2008. A spatial regularization approach to parameter estimation for a distributed watershed model. *Water Resources Research*, 44(12). <https://doi.org/10.1029/2007WR006615>
- Qin, Y., Abatzoglou, J.T., Siebert, S., Huning, L.S., AghaKouchak, A., Mankin, J.S., Hong, C., Tong, D., Davis, S.J. and Mueller, N.D., 2020. Agricultural risks from changing snowmelt. *Nature Climate Change*, 10(5), pp.459-465. <https://doi.org/10.1038/s41558-020-0746-8>
- Revuelto, J., Billecocq, P., Tuzet, F., Cluzet, B., Lamare, M., Larue, F. and Dumont, M., 2020. Random forests as a tool to understand the snow depth distribution and its evolution in mountain areas. *Hydrological Processes*. <https://doi.org/10.1002/hyp.13951>
- Robinson, D.A., Dewey, K.F. and Heim Jr, R.R., 1993. Global snow cover monitoring: An update. *Bulletin of the American Meteorological Society*, 74(9), pp.1689-1696. [https://doi.org/10.1175/1520-0477\(1993\)074<1689:GSCMAU>2.0.CO;2](https://doi.org/10.1175/1520-0477(1993)074<1689:GSCMAU>2.0.CO;2)
- Samaniego, L., Kumar, R. and Attinger, S., 2010. Multiscale parameter regionalization of a grid-based hydrologic model at the mesoscale. *Water Resources Research*, 46(5). <https://doi.org/10.1029/2008WR007327>
- Shen, C., 2018. A transdisciplinary review of deep learning research and its relevance for water resources scientists. *Water Resources Research*, 54(11), pp.8558-8593. <https://doi.org/10.1029/2018WR022643>
- Shen, C., Laloy, E., Elshorbagy, A., Albert, A., Bales, J., Chang, F.J., Ganguly, S., Hsu, K.L., Kifer, D., Fang, Z. and Fang, K., 2018. HESS Opinions: Incubating deep-learning-powered

hydrologic science advances as a community. *Hydrology and Earth System Sciences*, 22(11), pp.5639-5656. <https://doi.org/10.5194/hess-22-5639-2018>

Schaefli, B. and Gupta, H.V., 2007. Do Nash values have value?. *Hydrological Processes*, 21(ARTICLE), pp.2075-2080. <https://doi.org/10.1002/hyp.6825>

Schaefli, B., Hingray, B., Niggli, M. and Musy, A., 2005. A conceptual glacio-hydrological model for high mountainous catchments. *Hydrology and earth system sciences*, 9(1/2), pp.95-109. <https://doi.org/10.5194/hess-9-95-2005>

Schoups, G., Van de Giesen, N.C. and Savenije, H.H.G., 2008. Model complexity control for hydrologic prediction. *Water Resources Research*, 44(12). <https://doi.org/10.1029/2008WR006836>

Shindell, D., Kuylenstierna, J.C., Vignati, E., van Dingenen, R., Amann, M., Klimont, Z., Anenberg, S.C., Muller, N., Janssens-Maenhout, G., Raes, F. and Schwartz, J., 2012. Simultaneously mitigating near-term climate change and improving human health and food security. *Science*, 335(6065), pp.183-189. <https://doi.org/10.1126/science.1210026>

Simpkins, G., 2018. Snow-related water woes. *Nature Climate Change*, 8(11), pp.945-945. <https://doi.org/10.1038/s41558-018-0330-7>

Sivapalan, M., Takeuchi, K., Franks, S.W., Gupta, V.K., Karambiri, H., Lakshmi, V., Liang, X., McDonnell, J.J., Mendiondo, E.M., O'connell, P.E. and Oki, T., 2003. IAHS Decade on Predictions in Ungauged Basins (PUB), 2003–2012: Shaping an exciting future for the hydrological sciences. *Hydrological sciences journal*, 48(6), pp.857-880. <https://doi.org/10.1623/hysj.48.6.857.51421>

Snauffer, A.M., Hsieh, W.W., Cannon, A.J. and Schnorbus, M.A., 2018. Improving gridded snow water equivalent products in British Columbia, Canada: multi-source data fusion by neural network models. *The Cryosphere*, 12(3), pp.891-905. <https://doi.org/10.5194/tc-12-891-2018>

Strasser, U., Etchevers, P. and Lejeune, Y., 2002. Inter-Comparison of two Snow Models with Different Complexity using Data from an Alpine Site: Selected paper from EGS General Assembly, Nice, April-2000 (Symposium OA36). *Hydrology Research*, 33(1), pp.15-26. <https://doi.org/10.2166/nh.2002.0002>

Sudriani, Y., Ridwansyah, I. and Rustini, H.A., 2019, July. Long short-term memory (LSTM) recurrent neural network (RNN) for discharge level prediction and forecast in Cimandiri river, Indonesia. In *IOP Conference Series: Earth and Environmental Science* (Vol. 299, No. 1, p. 012037). IOP Publishing. <https://doi.org/10.1088/1755-1315/299/1/012037>

Swenson, S.C. and Lawrence, D.M., 2012. A new fractional snow-covered area parameterization for the Community Land Model and its effect on the surface energy balance. *Journal of geophysical research: Atmospheres*, 117(D21). <https://doi.org/10.1029/2012JD018178>

Tabari, H., Marofi, S., Abyaneh, H.Z. and Sharifi, M.R., 2010. Comparison of artificial neural network and combined models in estimating spatial distribution of snow depth and snow water equivalent in Samsami basin of Iran. *Neural Computing and Applications*, 19(4), pp.625-635. <https://doi.org/10.1007/s00521-009-0320-9>

Tarboton, D.G. and Luce, C.H., 1996. *Utah energy balance snow accumulation and melt model (UEB)*. Utah Water Research Laboratory.

- Tribbeck, M. J., R. J. Gurney, E. M. Morris, and D. W. C. Pearson (2004), A new snow-SVAT to simulate the accumulation and ablation of seasonal snow cover beneath a forest canopy, *J. Glaciol.*, **50**, 171–182. <https://doi.org/10.3189/172756504781830187>
- Wang, Y.H., Broxton, P., Fang, Y., Behrangi, A., Barlage, M., Zeng, X. and Niu, G.Y., 2019. A wet-bulb temperature-based rain-snow partitioning scheme improves snowpack prediction over the drier western United States. *Geophysical Research Letters*, *46*(23), pp.13825-13835. <https://doi.org/10.1029/2019GL085722>
- Weijis, S.V. and Ruddell, B.L., 2020. Debates: Does information theory provide a new paradigm for earth science? Sharper predictions using Occam's digital razor. *Water Resources Research*, *56*(2). <https://doi.org/10.1029/2019WR026471>
- Welty, J. and Zeng, X., 2021. Characteristics and Causes of Extreme Snowmelt over the Conterminous United States. *Bulletin of the American Meteorological Society*, pp.1-37. <https://doi.org/10.1175/BAMS-D-20-0182.1>
- Westerling, A.L., 2016. Increasing western US forest wildfire activity: sensitivity to changes in the timing of spring. *Philosophical Transactions of the Royal Society B: Biological Sciences*, *371*(1696), p.20150178. <https://doi.org/10.1098/rstb.2015.0178>
- Wunsch, A., Liesch, T. and Broda, S., 2021. Groundwater level forecasting with artificial neural networks: a comparison of long short-term memory (LSTM), convolutional neural networks (CNNs), and non-linear autoregressive networks with exogenous input (NARX). *Hydrology and Earth System Sciences*, *25*(3), pp.1671-1687. <https://doi.org/10.5194/hess-25-1671-2021>
- Xia, Y., Ek, M., Wei, H. and Meng, J., 2012. Comparative analysis of relationships between NLDAS-2 forcings and model outputs. *Hydrological Processes*, *26*(3), pp.467-474. <https://doi.org/10.1002/hyp.8240>
- Xiao, M., 2021. A warning of earlier snowmelt. *Nature Climate Change*, pp.1-2 <https://doi.org/10.1038/s41558-021-01024-7>
- Yosinski, J., Clune, J., Bengio, Y. and Lipson, H., 2014. How transferable are features in deep neural networks?. *arXiv preprint arXiv:1411.1792*

Figures

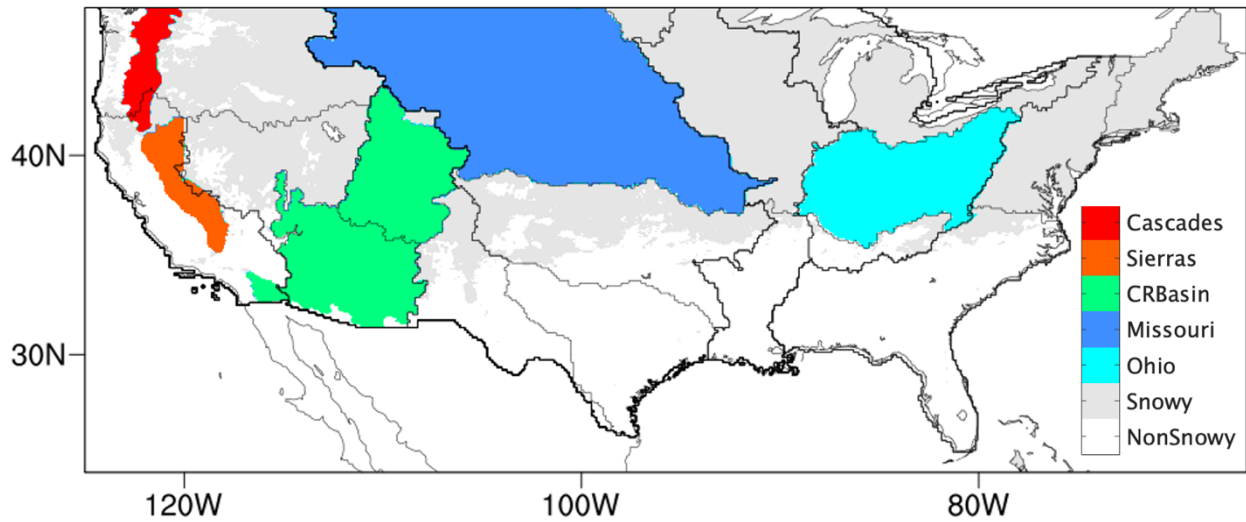


Figure 1. Geographic locations of five US regions include two Hydrologic Unit Code 2 (HUC2) basins (Ohio and Missouri) and three other regions in western CONUS (Colorado River Basin, Sierra Nevada and Cascades). The “snowy” pixels are shaded gray and the non-snowy pixels are shaded white. Sierras = Sierra Nevada; CRBasin = Colorado River Basin.

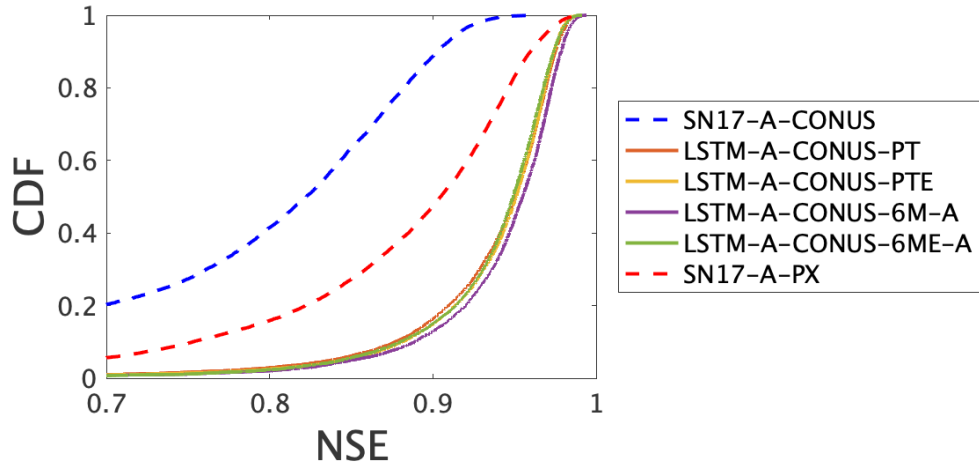


Figure 2. Aggregate NSE performance for the LSTM networks (solid lines) and the benchmark SN 17 models (dashed lines) when applied to the 15,000 pixels from *Pixel Set A*

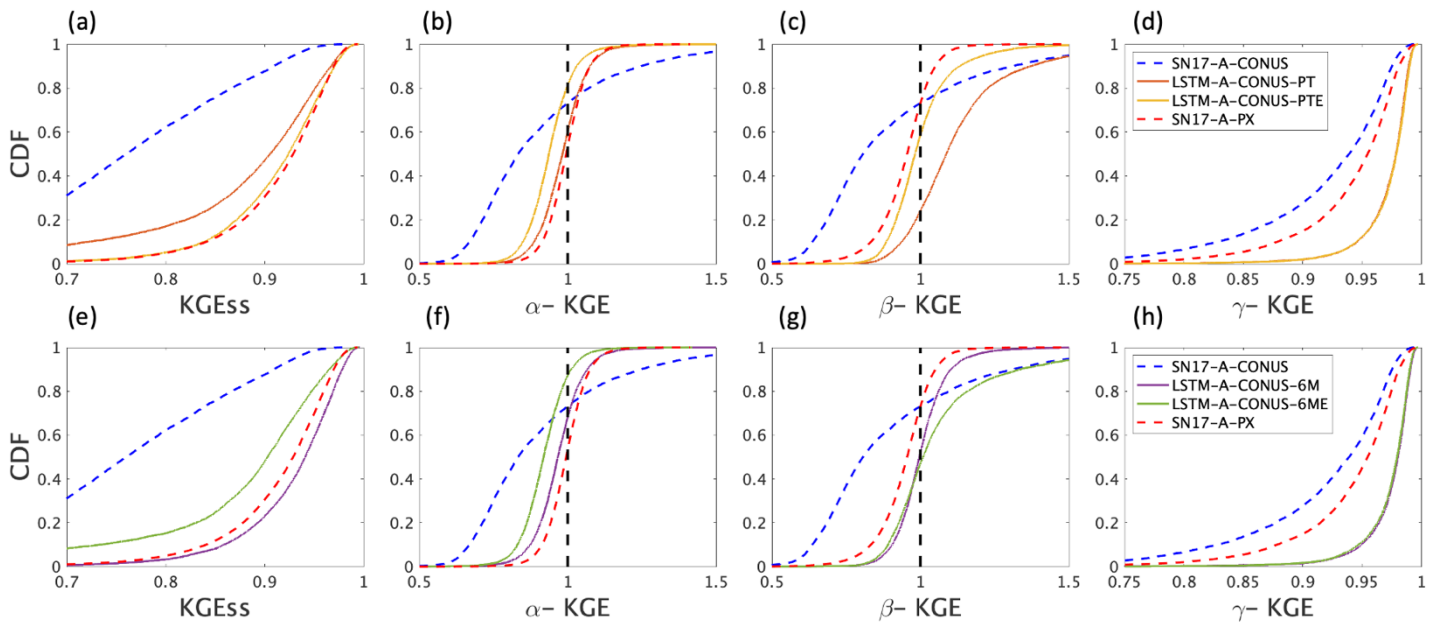


Figure 3. Aggregate performance, in terms of KGEss and the three KGE components, for the LSTM networks (solid lines) and the benchmark SN 17 models (dashed lines) when applied to the 15,000 pixels from *Pixel Set A*

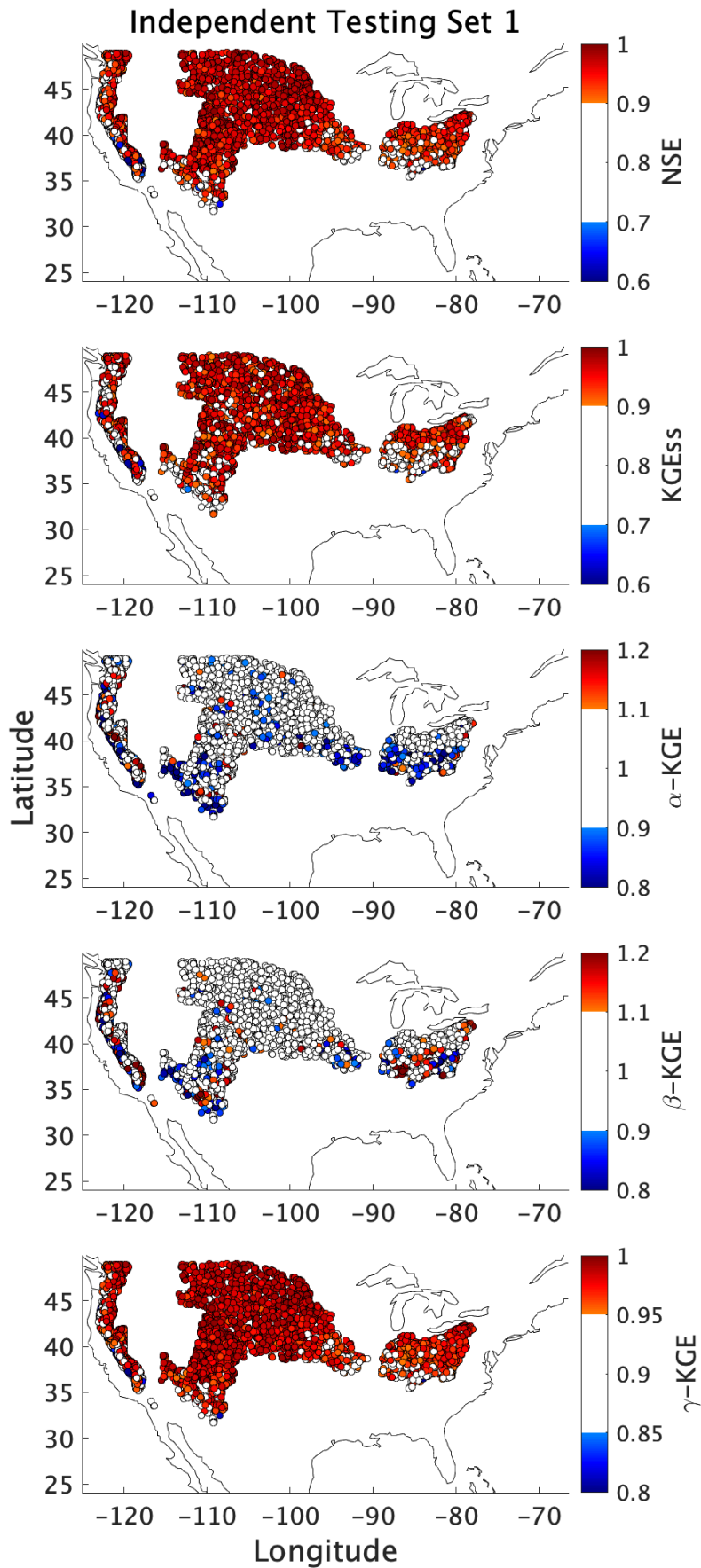


Figure 4. Spatial map indicating skill of the *LSTM-A-CONUS-6M* model (trained on *Pixel Set A*) when tested on an independent testing pixel set from *Pixel Set B*

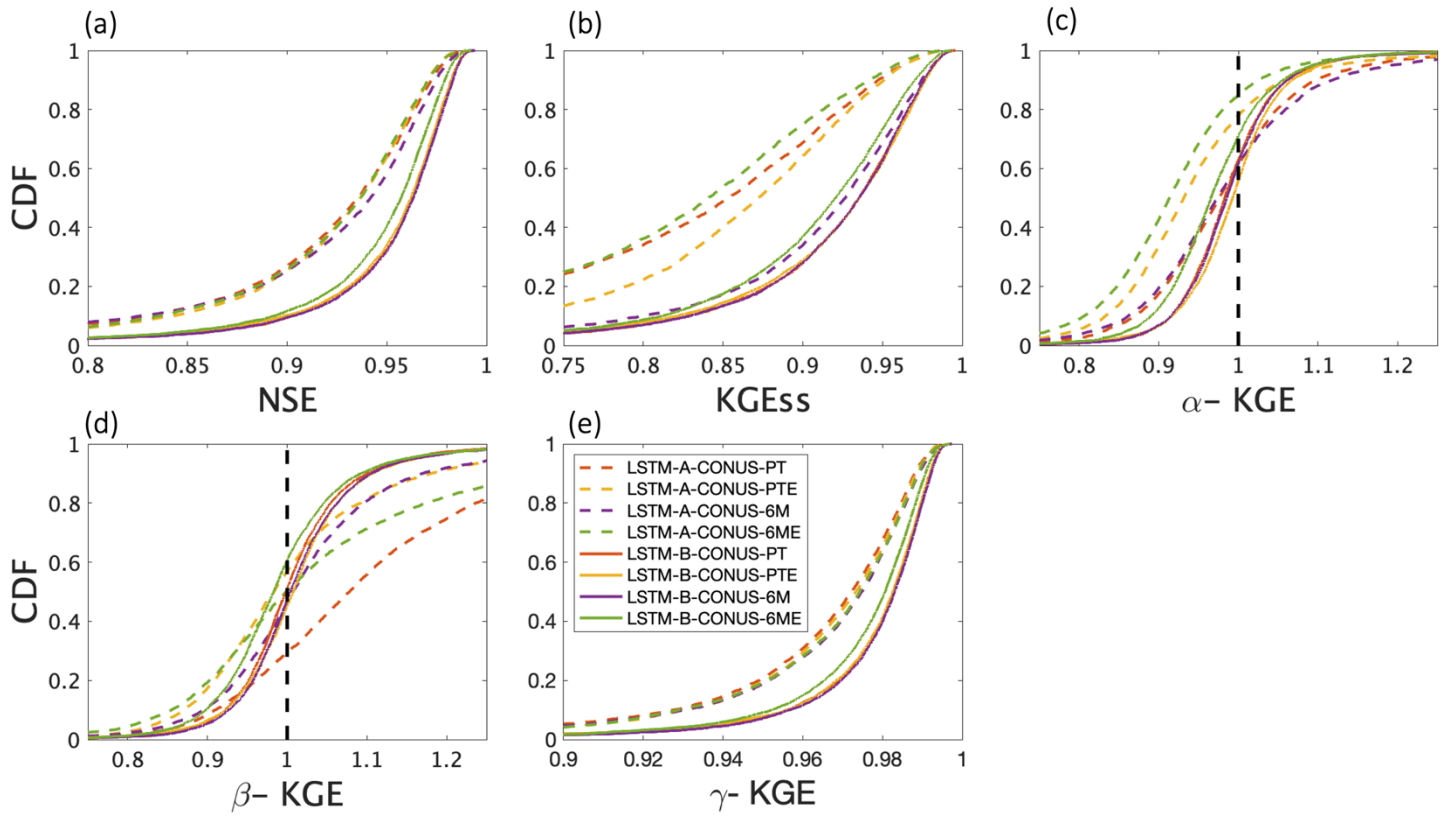


Figure 5. Aggregate performance of the trained CONUS-wide LSTM networks after fine-tuning using *Pixel Set B* compared to when pre-trained using *Pixel Set A*, where the evaluation is conducted over 5,000 independent testing pixels from *Pixel Set B*

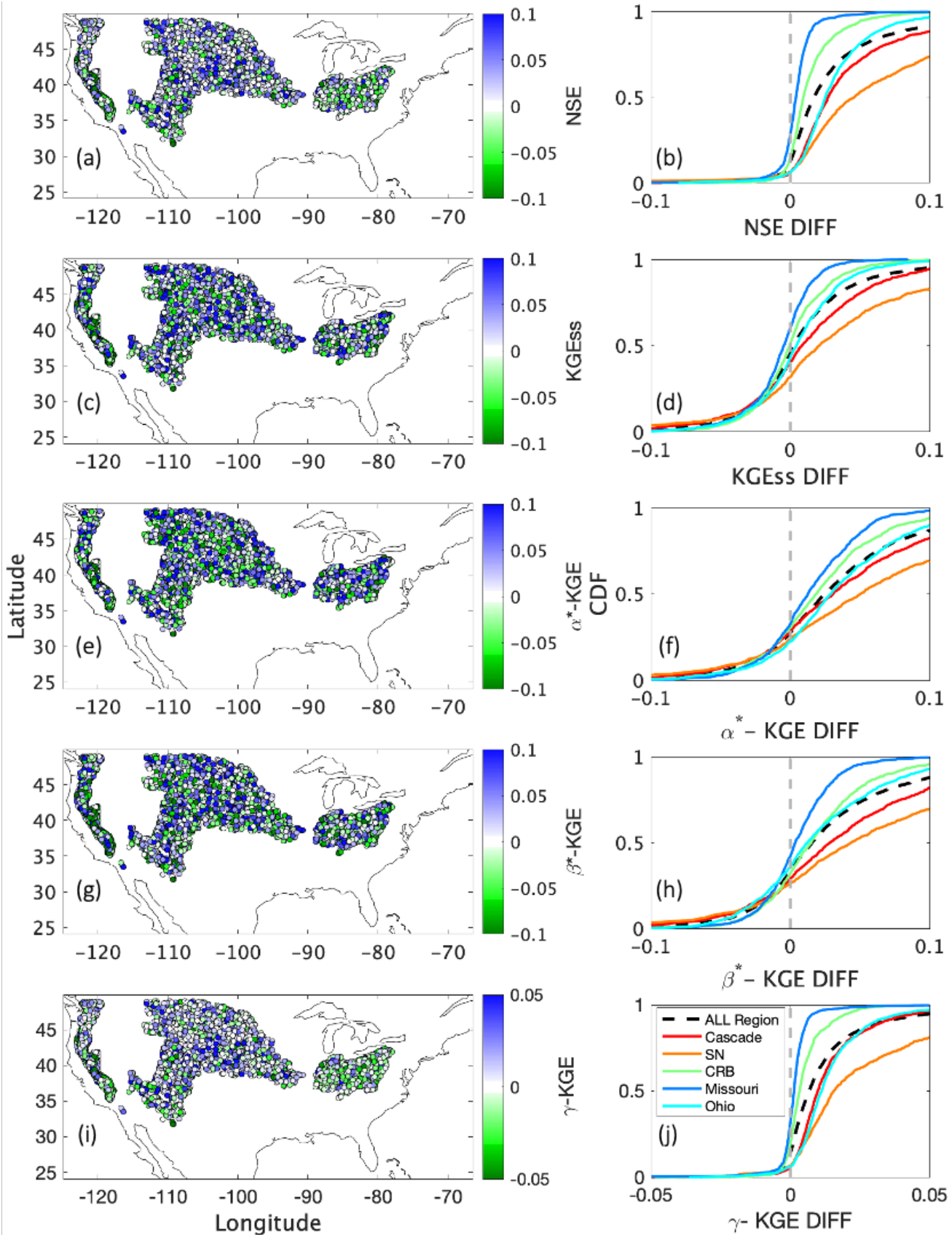


Figure 6. Difference in model skill between the CONUS-wide LSTMs trained on *Pixel Set B* and *Pixel Set A*, when using the 6 meteorological variables, evaluated over the 5,000 testing pixels from *Pixel Set B*. Note that $\alpha^* = 1 - |1 - \alpha|$, $\beta^* = 1 - |1 - \beta|$. Movement of the CDFs to the right (to more positive values) indicate that the *LSTM-B-CONUS* models have better performance than the corresponding *LSTM-A-CONUS* models

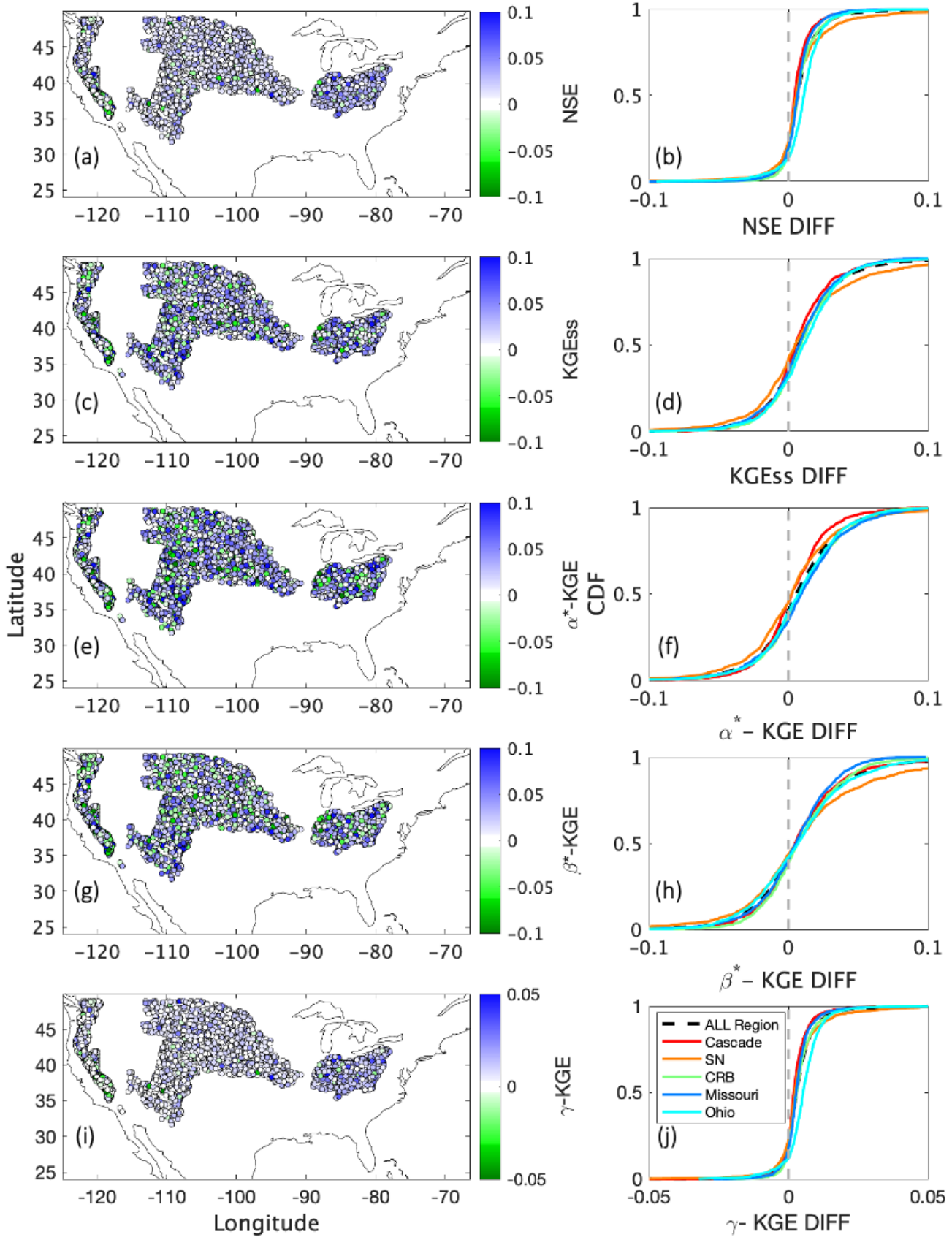


Figure 7. Difference in model skill between the regional LSTM and CONUS-wide LSTMs trained on Pixel Set B, when using the 6 meteorological variables, evaluated over the 5,000 testing pixels from *Pixel Set B*. Note that $\alpha^* = 1 - |1 - \alpha|$, $\beta^* = 1 - |1 - \beta|$. Movement of the CDFs to the right (to more positive values) indicates that the *LSTM-B-Region* models have better performance than the corresponding *LSTM-B-CONUS* models

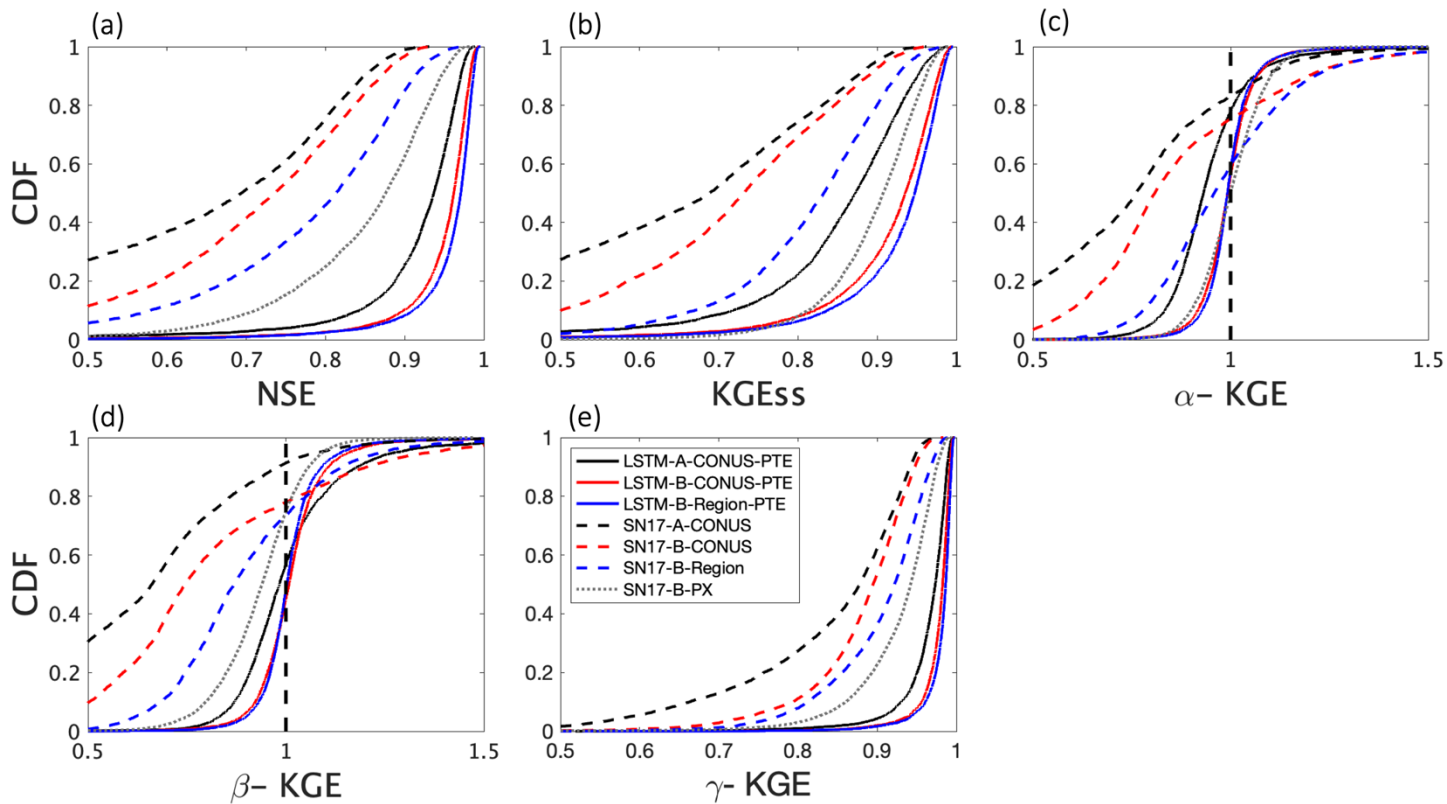


Figure 8. Aggregate performance of the LSTM models (solid lines) benchmarked against the SN17 models (dashed lines) when both are given the same input information (precipitation, temperature and elevation), evaluated over the 5,000 testing pixels from *Pixel Set B*

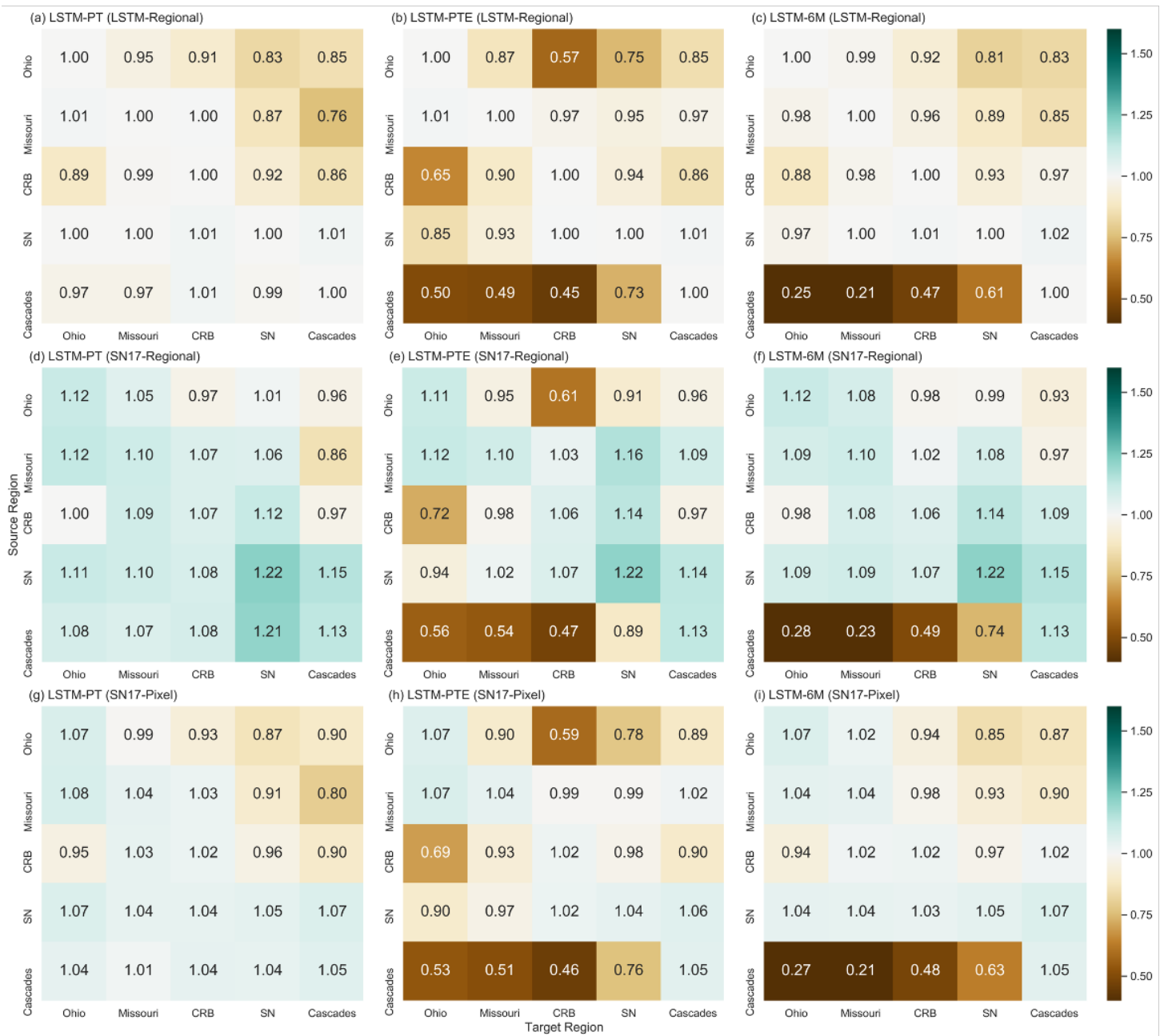


Figure 9. Results of the transfer learning experiments. In the top row the transferred LSTM networks are compared to their local-region trained counterparts. In the middle row, the transferred LSTM networks are compared to the corresponding local-region-trained SN17 models. In the bottom row, the transferred LSTM networks are compared to the corresponding local-pixel-trained SN17 models. Values larger than 1.0 indicate good relative performance of the transferred LSTM models.

Tables

Table 1. Parameters for the SNOW17 model summarized by *He et al. (2011a,b)* with ranges estimated from *Anderson (1973)*

Parameters	Explanation	Unit	Range
SCF	Snow fall correction factor	-	0.7-1.4
MFMAX	Maximum melt factor	mm per 6 h per C°	0.5-2.0
MFMIN	Minimum melt factor	mm per 6 h per C°	0.05-0.49
UADJ	The average wind function during rain-on-snow periods	mm per mbar per C°	0.03-0.19
NMF	Maximum negative melt factor	mm per 6 h per C°	0.05-0.50
MBASE	Base temperature for non-rain melt factor	C°	0.0-1.0
PXTEMP	Temperature that separates rain from snow	C°	-2.0-2.0
PLWHC	Percent of liquid water capacity	-	0.02-0.3
DAYGM	Daily melt at snow-soil interface	$mm\ d^{-1}$	0.0-0.3
TIPM	Antecedent snow temperature index parameter	-	0.1-1.0

Table 2. Summary statistics for the *LSTM-A-CONUS-6M* model evaluation results over *Pixel Set B*

Evaluation over Pixel Set B				
Model Skill	Percentage of Pixels for Independent Test Set 1	Percentage of Pixels for Independent Test Set 2	Percentage of Pixels for Independent Test Set 3	Percentage of Pixels for All Test Sets
$ \alpha - KGE > 10\%$	31.92%	31.74%	31.40%	31.69%
$ \beta - KGE > 10\%$	30.24%	30.20%	30.22%	30.22%
$\gamma - KGE > 0.95$	82.08%	82.42%	80.92%	81.81%
$KGE_{ss} > 0.95$	32.72%	30.84%	31.06%	31.54%
$NSE > 0.95$	41.18%	40.34%	41.84%	41.12%
$\gamma - KGE < 0.85$	2.20%	1.96%	1.88%	2.01%
$KGE_{ss} < 0.70$	3.96%	3.90%	4.22%	4.03%
$NSE < 0.70$	3.72%	3.70%	3.70%	3.71%

Table 3. Summary of SWE hydrograph pairwise correlation statistics over *Pixel Set B*

SWE Pairwise Correlation for Pixel Set B (WY1982-2000)					
Regions	Statistics	Independent Test set 1	Independent Test Set 2	Independent Test Set 3	All Pixels
Ohio	Mean	0.59	0.59	0.60	0.60
	Median	0.56	0.60	0.60	0.60
	Stdev	0.17	0.17	0.17	0.17
Missouri	Mean	0.46	0.47	0.47	0.47
	Median	0.47	0.48	0.49	0.48
	Stdev	0.19	0.19	0.19	0.19
CRB	Mean	0.48	0.47	0.47	0.47
	Median	0.48	0.48	0.48	0.48
	Stdev	0.23	0.23	0.23	0.23
SN	Mean	0.52	0.54	0.52	0.53
	Median	0.51	0.53	0.52	0.52
	Stdev	0.25	0.25	0.25	0.25
Cascades	Mean	0.55	0.53	0.54	0.54
	Median	0.54	0.52	0.53	0.53
	Stdev	0.24	0.24	0.24	0.24